Received: 13 November 2019 | Revised: 12 February 2020 | Accepted: 4 May 2020

DOI: 10.1002/nme.6428

SPECIAL ISSUE ARTICLE

WILEY

A second-order face-centred finite volume method on general meshes with automatic mesh adaptation

Matteo Giacomini[1] | **Ruben Sevilla**[2]

[1]Laboratori de Càlcul Numèric (LaCàN), ETS de Ingenieros de Caminos, Canales y Puertos, Universitat Politècnica de Catalunya, Barcelona, Spain

[2]Zienkiewicz Centre for Computational Engineering, College of Engineering, Swansea University, Swansea, UK

Correspondence
Ruben Sevilla, Zienkiewicz Centre for Computational Engineering, College of Engineering, Swansea University, Bay Campus, SA1 8EN, Swansea, Wales, UK.
Email: r.sevilla@swansea.ac.uk

Funding information
Agència de Gestió d'Ajuts Universitaris i de Recerca, Grant/Award Number: 2017-SGR-1278; Engineering and Physical Sciences Research Council, Grant/Award Number: EP/P033997/1; H2020 Marie Skłodowska-Curie Actions, Grant/Award Number: 764636; Secretaría de Estado de Investigación, Desarrollo e Innovación, Grant/Award Number: DPI2017-85139-C2-2-R

Summary

A second-order face-centred finite volume strategy on general meshes is proposed. The method uses a mixed formulation in which a constant approximation of the unknown is computed on the faces of the mesh. Such information is then used to solve a set of problems, independent cell-by-cell, to retrieve the local values of the solution and its gradient. The main novelty of this approach is the introduction of a new basis function, utilised for the linear approximation of the primal variable in each cell. Contrary to the commonly used nodal basis, the proposed basis is suitable for computations on general meshes, including meshes with different cell types. The resulting approach provides second-order accuracy for the solution and first-order for its gradient, without the need of reconstruction procedures, is robust in the incompressible limit and insensitive to cell distortion and stretching. The second-order accuracy of the solution is exploited to devise an automatic mesh adaptivity strategy. An efficient error indicator is obtained from the computation of one extra local problem, independent cell-by-cell, and is used to drive mesh adaptivity. Numerical examples illustrating the approximation properties of the method and of the mesh adaptivity procedure are presented. The potential of the proposed method with automatic mesh adaptation is demonstrated in the context of microfluidics.

KEYWORDS

automatic adaptivity, face-centred, finite volume methods, general meshes, hybridisable discontinuous Galerkin, second-order

1 | INTRODUCTION

Finite volume (FV) methods are one of the most popular computational methods for solving systems of conservation laws.[1-4] These methods are usually classified into two families, namely, cell-centred FVs and vertex-centred FVs depending on the definition of the unknowns at the centroids or at the vertices of the cells, respectively. The main attractive properties of FV methods are their numerical efficiency, local conservation, and robustness which make them appealing solutions to treat flow problems of industrial interest.[5-7] However, one of the drawbacks of low-order cell-centred and vertex-centred FVs is the need for a reconstruction of the gradient. In this context, the quality of the reconstruction is directly linked to the quality of the mesh. A mesh with highly

distorted or stretched cells usually leads to an important loss of accuracy, and in some cases, a loss of the second-order convergence.[8,9]

A new class of FV methods, named as face-centred finite volume (FCFV) method, was recently introduced in Reference 10. The method is based on the hybridisable discontinuous Galerkin (HDG) method by Cockburn et al[11-15] and defines the global unknowns on the cell faces (edges in two dimensions). The main attractive property of this scheme is the ability to produce a first-order accurate approximation of the solution and its gradient without the need of a reconstruction. Therefore, the method is insensitive to mesh distortion and cell stretching. In addition, the FCFV method inherits the convergence properties of HDG, it passes the LBB condition using equal-order approximations for velocity and pressure in the context of incompressible flows[16,17] and it is robust when solving linear elasticity problems in the incompressible limit.[18-20] The main drawback of this method is that, even for a sufficiently regular mesh, it provides a first-order approximation of the solution, compared with the second-order provided by cell-centred and vertex-centred FV methods.

In Reference 21 the authors proposed a second-order FCFV method with a computational cost almost identical to the cost of the original first-order FCFV method. The main idea is to use a piecewise linear approximation of the solution in the cells, but maintain a piecewise constant approximation for its gradient in the cells and for the solution on the cell faces. In addition, the method introduces a projection operator in the definition of the numerical fluxes, following the work of References 22-24. However, the second-order FCFV method proposed in Reference 21 is only applicable on simplicial meshes. Furthermore, the mesh adaptivity process proposed in Reference 21 is expensive as it requires the solution of two global problems to compute a local error indicator to drive the mesh adaptivity process.

This article proposes a modification of the recently proposed second-order FCFV method that enables the use of general and hybrid meshes. The key idea is to introduce a new approximation space for the primal variable that leads to second-order convergence on general meshes. The singularity induced by the use of nodal basis functions in nonsimplicial meshes is first illustrated and a set of linear basis functions is introduced to overcome this problem. The basis functions introduced have been previously used in other numerical schemes,[25] but not in the context of the FCFV method, enabling the application of this recently proposed scheme to problems where nonsimplicial meshes are preferred. Numerical examples involving triangular and quadrilateral cells in two dimensions and tetrahedral, hexahedral, prismatic, and pyramidal cells in three dimensions are presented to demonstrate the optimal convergence properties of the method in the context of second-order elliptic problems.

In addition, this article proposes an efficient error indicator to drive a mesh adaptivity process. It is worth noting that the FCFV, contrary to higher order HDG methods, lacks the ability to provide a superconvergent solution and therefore other strategies are required to devise an error indicator. Contrary to the error indicator proposed in Reference 21, the present strategy does not require the solution of two global problems and only involves local quantities. More precisely, the proposed error indicator only requires cell-by-cell calculations and therefore can be easily computed in parallel.

The remainder of this article is organised as follows. The rationale of the second-order FCFV method is recalled in Section 2 for a scalar second-order elliptic problem. After introducing the new basis functions required for general and hybrid meshes, the novel second-order FCFV formulation for Poisson and Stokes equations is derived in Section 3. Section 4 proposes an efficient strategy to perform mesh adaptivity via the computation of an inexpensive local error indicator. Extensive numerical tests are discussed in Section 5 to validate the proposed method, in two and three dimensions, and to verify its optimal approximation properties for general and hybrid meshes. Section 6 presents the application of the proposed mesh adaptivity strategy to a two-dimensional (2D) thermal problem using both triangular and quadrilateral meshes and to an incompressible Stokes flow around a complex three-dimensional (3D) geometry of a microswimmer. Eventually, Section 7 summarises the main results and novelties of the article.

2 | FUNDAMENTALS OF THE SECOND-ORDER FCFV METHOD

This section briefly recalls the second-order FCFV method introduced in Reference 21. To simplify the presentation, the method is described using the Poisson equation as a model problem.

2.1 | Problem statement and mixed formulation

An open bounded domain $\Omega \in \mathbb{R}^{\mathtt{n_{sd}}}$ is considered, where $\mathtt{n_{sd}}$ denotes the number of spatial dimensions. The boundary of the domain is split into the nonoverlapping Dirichlet boundary, Γ_D, where the solution is known, and the Neumann boundary, Γ_N, where the normal flux is known.

The computational domain is assumed to be partitioned in $\mathtt{n_e}$ nonoverlapping cells Ω_e, for $e = 1,\dots,\mathtt{n_e}$. The boundary of each cell is expressed as the union of a set of faces (edges in two dimensions), Γ_{ej}, for $j = 1,\dots,\mathtt{n_f^e}$, where $\mathtt{n_f^e}$ denotes the number of faces (edges in two dimensions) of the cell Ω_e.

The FCFV method considers the strong form of the Poisson equation written in mixed form, via the introduction of the variable $\boldsymbol{q}$, and in a cell-by-cell fashion, namely

$$\begin{cases} \boldsymbol{q} + \boldsymbol{\nabla} u = \boldsymbol{0} & \text{in } \Omega_e, \text{ and for } e = 1,\dots,\mathtt{n_e}, \\ \boldsymbol{\nabla}\cdot\boldsymbol{q} = s & \text{in } \Omega_e, \text{ and for } e = 1,\dots,\mathtt{n_e}, \\ u = u_D & \text{on } \partial\Omega_e \cap \Gamma_D, \\ \boldsymbol{n}\cdot\boldsymbol{q} = -t & \text{on } \partial\Omega_e \cap \Gamma_N, \\ [\![u\boldsymbol{n}]\!] = \boldsymbol{0} & \text{on } \Gamma, \\ [\![\boldsymbol{n}\cdot\boldsymbol{q}]\!] = 0 & \text{on } \Gamma. \end{cases} \tag{1}$$

where s is a source term, $\boldsymbol{n}$ is the outward unit normal to the boundary, u_D is the known value of the solution on the Dirichlet boundary, t is the known value of the flux on the Neumann boundary and Γ, defined by

$$\Gamma := \left[\bigcup_{e=1}^{\mathtt{n_e}} \partial\Omega_e \right] \setminus \partial\Omega \tag{2}$$

is the so-called *internal mesh skeleton*.

It is worth noting that the last two equations in (1) impose the continuity of the solution and the normal flux, respectively, across the internal faces of the mesh, the *jump operator* being defined as

$$[\![\odot]\!] = \odot_l + \odot_r, \tag{3}$$

that is, the sum of the quantity inside the left and right cell, Ω_l and Ω_r, respectively, sharing a face of the mesh skeleton.[26]

2.2 | Strong form of the local and global problems

Following the standard rationale of HDG[15,27-30] and FCFV[10,20,21] methods, the strong mixed form (1) is split into the so-called local and global problems. The local problems are defined independently in each cell as

$$\begin{cases} \boldsymbol{q}_e + \boldsymbol{\nabla} u_e = \boldsymbol{0} & \text{in } \Omega_e, \\ \boldsymbol{\nabla}\cdot\boldsymbol{q}_e = s & \text{in } \Omega_e, \\ u_e = u_D & \text{on } \partial\Omega_e \cap \Gamma_D, \\ u_e = \hat{u} & \text{on } \partial\Omega_e \setminus \Gamma_D, \end{cases} \tag{4}$$

for $e = 1,\dots,\mathtt{n_e}$. It is worth noting that each local problem contains only Dirichlet boundary conditions and it introduces a new independent variable, $\hat{u}$, called the *hybrid* variable that corresponds to the solution at the cell faces (edges in two dimensions).

The global problem is defined on the mesh skeleton and the Neumann boundary as

$$\begin{cases} [\![u\boldsymbol{n}]\!] = \boldsymbol{0} & \text{on } \Gamma, \\ [\![\boldsymbol{n}\cdot\boldsymbol{q}]\!] = 0 & \text{on } \Gamma, \\ \boldsymbol{n}\cdot\boldsymbol{q} = -t & \text{on } \Gamma_N. \end{cases} \tag{5}$$

The first equation in (5) can be henceforth omitted because the continuity of the solution is automatically satisfied due to the imposition of the Dirichlet boundary condition in the local problems and to the uniqueness of the hybrid variable on Γ.

2.3 | Weak form of the local and global problems

The recently proposed second-order FCFV[21] introduces a linear approximation of the primal variable in each cell, u_e^h, and a piecewise constant approximation of the mixed and hybrid variables, $\boldsymbol{q}_e^h$ and $\hat{u}^h$, respectively.

The weak formulation of the local problem in each cell is: find $(u_e^h, \boldsymbol{q}_e^h) \in \mathcal{V}^1(\Omega_e) \times [\mathcal{V}^0(\Omega_e)]^{\mathrm{n_{sd}}}$ such that

$$-\int_{\Omega_e} \boldsymbol{q}_e^h d\Omega = \int_{\partial\Omega_e \cap \Gamma_D} u_D \boldsymbol{n}_e d\Gamma + \int_{\partial\Omega_e \setminus \Gamma_D} \hat{u}^h \boldsymbol{n}_e d\Gamma, \tag{6a}$$

$$-\int_{\Omega_e} \boldsymbol{\nabla} v \cdot \boldsymbol{q}_e^h d\Omega + \int_{\partial\Omega_e} v(\boldsymbol{n}_e \cdot \hat{\boldsymbol{q}}_e^h) d\Gamma = \int_{\Omega_e} v s d\Omega \tag{6b}$$

for all test functions $v \in \mathcal{V}^1(\Omega_e)$ and for $e = 1, \dots, \mathrm{n_e}$. Here, $\mathcal{V}^1(\Omega_e)$ is the space of at most linear functions in Ω_e and $\mathcal{V}^0(\Omega_e)$ is the space of constant functions in Ω_e. It is worth mentioning that the weak formulation (6a) is obtained by selecting an arbitrary test function in $[\mathcal{V}^0(\Omega_e)]^{\mathrm{n_{sd}}}$.

The numerical flux, $\hat{\boldsymbol{q}}_e^h$, introduced in (6b) is defined as

$$\boldsymbol{n}_e \cdot \hat{\boldsymbol{q}}_e^h := \begin{cases} \boldsymbol{n}_e \cdot \boldsymbol{q}_e^h + \tau_e(\mathbb{P}_0 u_e^h - u_D) & \text{on } \partial\Omega_e \cap \Gamma_D, \\ \boldsymbol{n}_e \cdot \boldsymbol{q}_e^h + \tau_e(\mathbb{P}_0 u_e^h - \hat{u}^h) & \text{elsewhere,} \end{cases} \tag{7}$$

where $\tau_e > 0$ is the so-called *stabilisation parameter*[15,27-30] and, similar to References 22,23, the projection operator $\mathbb{P}_0$ over the space of constant functions is introduced.

Remark 1. As discussed in Reference 21, the two ingredients required to obtain a second-order FCFV method are the use of piecewise linear functions to approximate the primal variable and the introduction of the projection operator in the definition of the numerical flux.

The weak formulation of the local problems is obtained after introducing the definition of the numerical flux into (6b), performing an integration by parts of the first term and exploiting that $\boldsymbol{\nabla} \cdot \boldsymbol{q}_e^h = 0$, being $\boldsymbol{q}_e^h$ a piecewise constant function in each cell Ω_e. Hence, it reads: find $(u_e^h, \boldsymbol{q}_e^h) \in \mathcal{V}^1(\Omega_e) \times [\mathcal{V}^0(\Omega_e)]^{\mathrm{n_{sd}}}$ such that

$$-\int_{\Omega_e} \boldsymbol{q}_e^h d\Omega = \int_{\partial\Omega_e \cap \Gamma_D} u_D \boldsymbol{n}_e d\Gamma + \int_{\partial\Omega_e \setminus \Gamma_D} \hat{u}^h \boldsymbol{n}_e d\Gamma, \tag{8a}$$

$$\int_{\partial\Omega_e} v \tau_e \mathbb{P}_0 u_e^h d\Gamma = \int_{\Omega_e} v s d\Omega + \int_{\partial\Omega_e \cap \Gamma_D} v \tau_e u_D d\Gamma + \int_{\partial\Omega_e \setminus \Gamma_D} v \tau_e \hat{u}^h d\Gamma \tag{8b}$$

for all $v \in \mathcal{V}^1(\Omega_e)$ and for $e = 1, \dots, \mathrm{n_e}$.

The weak formulation of the global problem is derived by following a similar procedure. It reads: find $\hat{u}^h \in \hat{\mathcal{V}}^0(\Gamma \cup \Gamma_N)$ such that

$$\sum_{e=1}^{\mathrm{n_e}} \int_{\partial\Omega_e \setminus \Gamma_D} \boldsymbol{n}_e \cdot \hat{\boldsymbol{q}}_e^h d\Gamma = -\sum_{e=1}^{\mathrm{n_e}} \int_{\partial\Omega_e \cap \Gamma_N} t d\Gamma, \tag{9}$$

where an arbitrary test function has been selected from $\hat{\mathcal{V}}^0(\Gamma \cup \Gamma_N)$. By using the expression of the numerical flux introduced in (7), the discrete weak formulation becomes: find $\hat{u}^h \in \hat{\mathcal{V}}^0(\Gamma \cup \Gamma_N)$ such that

$$\sum_{e=1}^{\mathrm{n_e}} \int_{\partial\Omega_e \setminus \Gamma_D} \left(\boldsymbol{n}_e \cdot \boldsymbol{q}_e^h + \tau_e(\mathbb{P}_0 u_e^h - \hat{u}^h) \right) d\Gamma = -\sum_{e=1}^{\mathrm{n_e}} \int_{\partial\Omega_e \cap \Gamma_N} t d\Gamma. \tag{10}$$

2.4 | FCFV discretisation

Let us denote by $\mathcal{D}_e$ the set of faces of cell Ω_e on the Dirichlet boundary Γ_D and by $\mathcal{B}_e$ the set of faces of Ω_e in $\Gamma \cup \Gamma_N$, that is, the faces not on the Dirichlet boundary. Henceforth, the stabilisation parameter, Dirichlet and Neumann data are considered to assume constant values τ_j, $u_{D,j}$, and t_j, respectively, on each face/edge $\Gamma_{e,j}$ of the cell Ω_e.

The discrete local problem obtained from the weak form (8) provides an explicit expression of the primal and mixed variables in each cell as a function of the hybrid variable on the cell faces/edges, namely

$$\mathbf{q}_e = -|\Omega_e|^{-1}\mathbf{z}_e - |\Omega_e|^{-1}\sum_{j\in\mathcal{B}_e}|\Gamma_{e,j}|\boldsymbol{n}_j\hat{\mathrm{u}}_j, \tag{11a}$$

$$\mathbf{u}_e = \mathbf{m}_e^{-1}\mathbf{b}_e + \mathbf{m}_e^{-1}\sum_{j\in\mathcal{B}_e}\tau_j\mathbf{r}_j\hat{\mathrm{u}}_j, \tag{11b}$$

where $\mathbf{q}_e$ denotes the value of the mixed variable at the centroid of the cell and $\mathbf{u}_e$ denotes the nodal values of the primal variable. The right-hand side vectors depending on the problem data are defined as

$$\mathbf{b}_e := \mathbf{f}_e + \sum_{j\in\mathcal{D}_e}\tau_j\mathbf{d}_j, \quad \mathbf{z}_e := \sum_{j\in\mathcal{D}_e}|\Gamma_{e,j}|\boldsymbol{n}_j u_{D,j} \tag{12}$$

and the remaining matrices and vectors in the discrete equations are given by

$$(m_e)_{IJ} := \sum_{j=1}^{\mathrm{n_f^e}}(p_{e,j})_J\tau_j\frac{1}{\mathrm{n}_{\mathrm{fn}}^{e,j}}|\Gamma_{e,j}|\chi_{\mathcal{F}_{e,j}}(I), \quad (f_e)_I := \frac{1}{\mathrm{n_{en}}}s_e|\Omega_e|, \tag{13}$$

$$(d_j)_I := \frac{1}{\mathrm{n}_{\mathrm{fn}}^{e,j}}u_{D,j}|\Gamma_{e,j}|, \quad (r_j)_I := \frac{1}{\mathrm{n}_{\mathrm{fn}}^{e,j}}|\Gamma_{e,j}|\delta_{Ij}. \tag{14}$$

In the above expressions, $\mathrm{n_{en}}$ and $\mathrm{n_{fn}}$ are the numbers of nodes in each cell and face, respectively, and δ_{Ij} is the Kronecker delta. The vector $\mathbf{p}_{e,j}$, defined as

$$(p_{e,j})_I := \frac{1}{\mathrm{n}_{\mathrm{fn}}^{e,j}}\chi_{\mathcal{F}_{e,j}}(I), \tag{15}$$

is used to compute the projection of the primal variable from the space of linear to the one of constant polynomial functions. In addition, $\mathcal{F}_{e,k}$ denotes the set of nodes of the cell Ω_e that belong to the face $\Gamma_{e,k}$ and the indicator function of a set $\square$ is defined as

$$\chi_{\square}(I) = \begin{cases} 1 & \text{if } I \in \square \\ 0 & \text{otherwise.} \end{cases} \tag{16}$$

The discrete global problem obtained by plugging the explicit expressions (11) in the weak form (10) results in a global system of equations where the unknown vector corresponds to the hybrid variable at the cell faces/edges. It can be written as

$$\hat{\mathbf{K}}\hat{\mathbf{u}} = \hat{\mathbf{f}}, \tag{17}$$

where the global matrix $\hat{\mathbf{K}}$ and vector $\hat{\mathbf{f}}$ are the result of assembling the contribution from each cell, given by

$$\hat{K}_{i,j}^e := |\Gamma_{e,i}|\left(\tau_i\tau_j\mathbf{p}_{e,j}\cdot\left(\mathbf{m}_e^{-1}\mathbf{r}_j\right) - |\Omega_e|^{-1}|\Gamma_{e,j}|\boldsymbol{n}_i\cdot\boldsymbol{n}_j - \tau_i\delta_{ij}\right), \tag{18a}$$

$$\hat{f}_i^e := |\Gamma_{e,i}|\left(|\Omega_e|^{-1}\boldsymbol{n}_i\cdot\mathbf{z}_e - \tau_i\mathbf{p}_{e,i}\cdot\left(\mathbf{m}_e^{-1}\mathbf{b}_e\right) - t_i\ \chi_{\mathcal{N}_e}(i)\right), \tag{18b}$$

for $i,j \in \mathcal{B}_e$ and with δ_{ij} denoting the Kronecker delta.

3 | LINEAR APPROXIMATION FOR THE SECOND-ORDER FCFV ON GENERAL MESHES

The second-order FCFV method proposed in Reference 21, summarised in the previous section, employs nodal shape functions to define the approximation of the primal variable, namely

$$u_e^h(\boldsymbol{x}) = \sum_{J=1}^{\mathtt{n}_{\mathtt{en}}} N_J^e(\boldsymbol{x}) u_J^e, \tag{19}$$

where $\{N_J^e\}_{J=1}^{\mathtt{n}_{\mathtt{en}}}$ is the set of linear Lagrange polynomials in the cell Ω_e and u_J^e, for $J = 1,\dots,\mathtt{n}_{\mathtt{en}}$, are the corresponding nodal values of the unknown function.

This section shows that this approach is only applicable with simplicial (triangular and tetrahedral) cells and proposes a new approximation space for general polygons and polyhedrons in two and three dimensions, respectively. The proposed formulation is first presented for the Poisson equation introduced in Section 2, and is extended to Stokes equations in section 3.4.

3.1 | The second-order FCFV with nodal basis functions

Consider the Poisson model problem (1) in two dimensions. The matrix $\mathbf{m}_e$ used in the local problem to write the solution in the cell as a function of the solution on the faces can thus be computed analytically. For a triangular cell, and assuming a constant value of the stabilisation parameter τ_e for all the faces, the matrix is given by

$$\mathbf{m}_e = \frac{\tau_e}{4} \begin{bmatrix} |\Gamma_{e,1}| + |\Gamma_{e,3}| & |\Gamma_{e,1}| & |\Gamma_{e,3}| \\ |\Gamma_{e,1}| & |\Gamma_{e,2}| + |\Gamma_{e,1}| & |\Gamma_{e,2}| \\ |\Gamma_{e,3}| & |\Gamma_{e,2}| & |\Gamma_{e,3}| + |\Gamma_{e,2}| \end{bmatrix}. \tag{20}$$

This matrix is invertible, with determinant equal to $(\tau_e^3/16)|\Gamma_{e,1}||\Gamma_{e,2}||\Gamma_{e,3}|$.

In a similar fashion, assume a constant value of the stabilisation parameter τ_e for all the faces of a quadrilateral cell. Using a nodal approximation with bilinear Lagrange polynomials, the matrix is given by

$$\mathbf{m}_e = \frac{\tau_e}{4} \begin{bmatrix} |\Gamma_{e,1}| + |\Gamma_{e,4}| & |\Gamma_{e,1}| & 0 & |\Gamma_{e,4}| \\ |\Gamma_{e,1}| & |\Gamma_{e,2}| + |\Gamma_{e,1}| & |\Gamma_{e,2}| & 0 \\ 0 & |\Gamma_{e,2}| & |\Gamma_{e,3}| + |\Gamma_{e,2}| & |\Gamma_{e,3}| \\ |\Gamma_{e,4}| & 0 & |\Gamma_{e,3}| & |\Gamma_{e,4}| + |\Gamma_{e,3}| \end{bmatrix}. \tag{21}$$

Contrary to the matrix obtained in (20) for a triangular cell, the matrix $\mathbf{m}_e$ for a quadrilateral cell is singular and the local problem in (11) cannot be solved. Hence, in order to devise a second-order FCFV method suitable to handle quadrilateral cells in 2D and hexahedral, prismatic, and pyramidal cells in 3D, an alternative description of the primal variable needs to be considered.

3.2 | Linear basis functions for the second-order FCFV method

This work proposes the use of a linear approximation of the primal variable in each cell, irrespective of its shape. More precisely, the approximation of the primal variable is defined as

$$u_e^h(\boldsymbol{x}) = \sum_{J=1}^{M} \tilde{N}_J^e(\boldsymbol{x}) c_J^e, \tag{22}$$

where the number of terms of the expansion is selected as $M = \mathtt{n}_{\mathtt{sd}}+1$, $\{\tilde{N}_J^e\}_{J=1}^{M}$ is a set of basis functions that span the space of polynomials of, at most, degree one and c_J^e, for $J = 1,\dots,M$ are coefficients appropriately defined to describe the unknown function.

The following basis functions are proposed in this work

$$\tilde{N}_1^e(\boldsymbol{x}) = 1 \quad \text{and} \quad \tilde{N}_k^e(\boldsymbol{x}) = x_{k-1} - \overline{x}_{k-1}^e \quad \text{for } k = 2, \dots M. \tag{23}$$

where $\overline{\boldsymbol{x}}^e = (\overline{x}_1^e, \dots, \overline{x}_{\mathrm{n_{sd}}}^e)$ denotes the coordinates of the centroid of the cell Ω_e.

It is worth noting that other choices for the basis functions are possible. The choice made here ensures that the coefficients in the approximation (22) have a physical interpretation. More precisely, c_1^e is the value of the primal variable at the centroid of the cell, whereas each coefficient c_k^e, for $k = 2,\dots M$, corresponds to the value of the derivative of the primal variable in the x_k direction, at the centroid of the cell.

It is also worth mentioning that the approximation defined in Equation (22) with the basis functions in Equation (23) corresponds to a Taylor expansion approximation of the primal variable on the edges. Therefore, it would be possible to use this philosophy to extend this approach to higher order. However, it is important to note that for higher order approximations, a standard HDG rationale already provides the optimal approximation properties on general meshes.[31]

Remark 2. The proposed FCFV scheme that results from considering the new set of linear basis functions reduces to the original second-order FCFV in Reference 21 for triangular and tetrahedral cells as in both cases the basis functions span the space of polynomials of, at most, degree one.

3.3 | Second-order FCFV discretisation of the Poisson equation

Considering the approximation of the primal variable proposed in the previous section and a constant approximation of the mixed and hybrid variables, the discrete local problem obtained from the weak form (8) is

$$\mathbf{q}_e = -|\Omega_e|^{-1}\mathbf{z}_e - |\Omega_e|^{-1}\sum_{j\in\mathcal{B}_e} |\Gamma_{e,j}|\boldsymbol{n}_j\hat{\mathrm{u}}_j, \tag{24a}$$

$$\mathbf{u}_e = \tilde{\mathbf{m}}_e^{-1}\tilde{\mathbf{b}}_e + \tilde{\mathbf{m}}_e^{-1}\sum_{j\in\mathcal{B}_e} \tau_j\tilde{\mathbf{r}}_j\hat{\mathrm{u}}_j. \tag{24b}$$

It is worth noting that Equation (24a), expressing the mixed variable in terms of the hybrid variable, is identical to the discrete Equation (11a) of the original second-order FCFV, whereas Equation (24b) requires the following definitions

$$\tilde{\mathbf{b}}_e := \tilde{\mathbf{f}}_e + \sum_{j\in\mathcal{D}_e} \tau_j\tilde{\mathbf{d}}_j, \tag{25}$$

and

$$(\tilde{m}_e)_{IJ} := \sum_{j=1}^{\mathrm{n_f^e}} (\tilde{p}_{e,j})_J\tau_j\int_{\Gamma_{e,j}} \tilde{N}_I d\Gamma, \quad (\tilde{f}_e)_I := \int_{\Omega_e} \tilde{N}_I s d\Omega, \tag{26}$$

$$(\tilde{d}_j)_I := u_{D,j}\int_{\Gamma_{e,j}} \tilde{N}_I d\Gamma, \quad (\tilde{r}_j)_I := \int_{\Gamma_{e,j}} \tilde{N}_I d\Gamma. \tag{27}$$

The vector $\tilde{\mathbf{p}}_{e,j}$, given by

$$(\tilde{p}_{e,j})_1 = 1 \quad \text{and} \quad (\tilde{p}_{e,j})_k = \overline{x}_{k-1}^{e,j} - \overline{x}_{k-1}^e \quad \text{for } k = 2, \dots M \tag{28}$$

is introduced to compute the projection of the primal linear variable on the space of the constant functions over a face $\Gamma_{e,j}$, where $\overline{\boldsymbol{x}}^{e,j} = (\overline{x}_1^{e,j}, \dots, \overline{x}_{\mathrm{n_{sd}}}^{e,j})$ denotes the centroid of the face $\Gamma_{e,j}$.

Analogously, the discrete global problem obtained from the weak form (10) using the expressions of primal and mixed variable in (24), results in a global system of equations where the unknown vector corresponds to the hybrid variable at the cell faces/edges. It can be written as

$$\hat{\mathbf{K}}\hat{\mathbf{u}} = \hat{\mathbf{f}}, \tag{29}$$

where the global matrix $\hat{\mathbf{K}}$ and vector $\hat{\mathbf{f}}$ are the result of assembling the contribution from each cell, given by

$$\hat{K}^e_{i,j} := |\Gamma_{e,i}| \left(\tau_i \tau_j \tilde{\mathbf{p}}_{e,j} \cdot \left(\tilde{\mathbf{m}}_e^{-1} \tilde{\mathbf{r}}_j \right) - |\Omega_e|^{-1} |\Gamma_{e,j}| \boldsymbol{n}_i \cdot \boldsymbol{n}_j - \tau_i \delta_{ij} \right), \tag{30a}$$

$$\hat{f}^e_i := |\Gamma_{e,i}| \left(|\Omega_e|^{-1} \boldsymbol{n}_i \cdot \mathbf{z}_e - \tau_i \tilde{\mathbf{p}}_{e,i} \cdot \left(\tilde{\mathbf{m}}_e^{-1} \tilde{\mathbf{b}}_e \right) - t_i \ \chi_{\mathcal{N}_e}(i) \right), \tag{30b}$$

for $i,j \in \mathcal{B}_e$.

3.4 | Second-order FCFV discretisation of the Stokes equations

In this section, the procedure described above for the derivation of the second-order FCFV formulation of the Poisson problem is extended to Stokes equations. By introducing the mixed variable $\boldsymbol{L}$, the strong form of the mixed problem is written cell-by-cell as

$$\begin{cases} \boldsymbol{L} + \sqrt{\nu} \boldsymbol{\nabla} \boldsymbol{u} = \mathbf{0} & \text{in } \Omega_e \text{ and for } e = 1, \dots, \mathtt{n_e}, \\ \boldsymbol{\nabla} \cdot \left(\sqrt{\nu} \boldsymbol{L} + p \mathbf{I}_{\mathtt{n_{sd}}} \right) = \boldsymbol{s} & \text{in } \Omega_e \text{ and for } e = 1, \dots, \mathtt{n_e}, \\ \boldsymbol{\nabla} \cdot \boldsymbol{u} = 0 & \text{in } \Omega_e \text{ and for } e = 1, \dots, \mathtt{n_e}, \\ \boldsymbol{u} = \boldsymbol{u}_D & \text{on } \partial\Omega_e \cap \Gamma_D, \\ \boldsymbol{n} \cdot \left(\sqrt{\nu} \boldsymbol{L} + p \mathbf{I}_{\mathtt{n_{sd}}} \right) = -\boldsymbol{t} & \text{on } \partial\Omega_e \cap \Gamma_N, \\ [\![\boldsymbol{u} \otimes \boldsymbol{n}]\!] = \mathbf{0} & \text{on } \Gamma, \\ [\![\boldsymbol{n} \cdot \left(\sqrt{\nu} \boldsymbol{L} + p \mathbf{I}_{\mathtt{n_{sd}}} \right)]\!] = \mathbf{0} & \text{on } \Gamma, \end{cases} \tag{31}$$

with the solvability constraint for the uniqueness of pressure given by

$$\frac{1}{|\partial\Omega_e|} \int_{\partial\Omega_e} p_e d\Gamma = \rho_e, \tag{32}$$

where ρ_e is the mean value of the pressure on the boundary of the cell Ω_e.[32,33] As for the scalar problem, the last two equations in (31) impose the continuity of the velocity and the normal flux, respectively, across the internal faces of the mesh.

Following the rationale in References 10,21, an additional unknown, the hybrid velocity $\hat{\boldsymbol{u}}$, is introduced on the cell faces and the condition $\boldsymbol{u} = \hat{\boldsymbol{u}}$ is enforced on the boundary $\partial\Omega_e \backslash \Gamma_D$ for $e = 1, \dots, \mathtt{n_e}$. The weak formulation of the Stokes problem in each cell is: given $\boldsymbol{u}_D$ on $\partial\Omega_e \cap \Gamma_D$ and $\hat{\boldsymbol{u}}^h$ on $\partial\Omega_e \backslash \Gamma_D$, find $(\boldsymbol{u}^h_e, p^h_e, \boldsymbol{L}^h_e) \in [\mathcal{V}^1(\Omega_e)]^{\mathtt{n_{sd}}} \times \mathcal{V}^0(\Omega_e) \times [\mathcal{V}^0(\Omega_e)]^{\mathtt{n_{sd}} \times \mathtt{n_{sd}}}$ such that

$$-\int_{\Omega_e} \boldsymbol{L}^h_e d\Omega = \int_{\partial\Omega_e \cap \Gamma_D} \sqrt{\nu} \boldsymbol{n}_e \otimes \boldsymbol{u}_D d\Gamma + \int_{\partial\Omega_e \backslash \Gamma_D} \sqrt{\nu} \boldsymbol{n}_e \otimes \hat{\boldsymbol{u}}^h d\Gamma, \tag{33a}$$

$$\int_{\partial\Omega_e} \tau_e \boldsymbol{w} \cdot \mathbb{P}_0 \boldsymbol{u}^h_e d\Gamma = \int_{\Omega_e} \boldsymbol{w} \cdot \boldsymbol{s} d\Omega + \int_{\partial\Omega_e \cap \Gamma_D} \tau_e \boldsymbol{w} \cdot \boldsymbol{u}_D d\Gamma + \int_{\partial\Omega_e \backslash \Gamma_D} \tau_e \boldsymbol{w} \cdot \hat{\boldsymbol{u}}^h d\Gamma, \tag{33b}$$

$$\int_{\partial\Omega_e \backslash \Gamma_D} \hat{\boldsymbol{u}} \cdot \boldsymbol{n}_e d\Gamma + \int_{\partial\Omega_e \cap \Gamma_D} \boldsymbol{u}_D \cdot \boldsymbol{n}_e d\Gamma = 0, \tag{33c}$$

$$\frac{1}{|\partial\Omega_e|} \int_{\partial\Omega_e} p^h_e d\Gamma = \rho^h_e, \tag{33d}$$

for all test functions $\boldsymbol{w} \in [\mathcal{V}^1(\Omega_e)]^{\mathtt{n_{sd}}}$, where the definition of the numerical normal flux featuring the projection operator $\mathbb{P}_0$ is utilised

$$\boldsymbol{n}_e \cdot \left(\sqrt{\nu} \widehat{\boldsymbol{L}^h_e + p^h_e \mathbf{I}_{\mathtt{n_{sd}}}} \right) := \begin{cases} \boldsymbol{n}_e \cdot \left(\sqrt{\nu} \boldsymbol{L}^h_e + p^h_e \mathbf{I}_{\mathtt{n_{sd}}} \right) + \tau_e (\mathbb{P}_0 \boldsymbol{u}^h_e - \boldsymbol{u}_D) & \text{on } \partial\Omega_e \cap \Gamma_D, \\ \boldsymbol{n}_e \cdot \left(\sqrt{\nu} \boldsymbol{L}^h_e + p^h_e \mathbf{I}_{\mathtt{n_{sd}}} \right) + \tau_e (\mathbb{P}_0 \boldsymbol{u}^h_e - \hat{\boldsymbol{u}}^h) & \text{elsewhere.} \end{cases} \tag{34}$$

In Equation (33), $[\mathcal{V}^1(\Omega_e)]^{\mathtt{n_{sd}}}$ is the space of $\mathtt{n_{sd}}$ dimensional vectors whose components are at most linear functions in Ω_e, whereas $[\mathcal{V}^0(\Omega_e)]^{\mathtt{n_{sd}}\times\mathtt{n_{sd}}}$ and $\mathcal{V}^0(\Omega_e)$ are the spaces of constant $\mathtt{n_{sd}}\times\mathtt{n_{sd}}$ tensorial and scalar functions in the cell Ω_e, respectively. It is worth mentioning that the weak formulations in Equations (33a) and (33c) are obtained by selecting an arbitrary constant test function in the spaces $[\mathcal{V}^0(\Omega_e)]^{\mathtt{n_{sd}}\times\mathtt{n_{sd}}}$ and $\mathcal{V}^0(\Omega_e)$, respectively.

The weak formulation of the global problem is derived in a similar way by imposing Neumann and transmission conditions on Γ_N and Γ, respectively, and a compatibility condition for the incompressiblity constraint in each cell Ω_e, for $e=1,\dots,\mathtt{n_e}$. It reads: find $(\hat{\boldsymbol{u}}^h, \rho_e^h) \in [\hat{\mathcal{V}}^0(\Gamma\cup\Gamma_N)]^{\mathtt{n_{sd}}}\times\mathbb{R}$ such that

$$\sum_{e=1}^{\mathtt{n_e}} \int_{\partial\Omega_e\setminus\Gamma_D} \left(\sqrt{\nu}\boldsymbol{n}_e\cdot\boldsymbol{L}_e^h + p_e^h\boldsymbol{n}_e + \tau_e(\mathbb{P}_0\boldsymbol{u}_e^h - \hat{\boldsymbol{u}}^h)\right) d\Gamma = -\sum_{e=1}^{\mathtt{n_e}} \int_{\partial\Omega_e\cap\Gamma_N} \boldsymbol{t} d\Gamma, \tag{35a}$$

$$\int_{\partial\Omega_e\setminus\Gamma_D} \hat{\boldsymbol{u}}\cdot\boldsymbol{n}_e d\Gamma + \int_{\partial\Omega_e\cap\Gamma_D} \boldsymbol{u}_D\cdot\boldsymbol{n}_e d\Gamma = 0 \quad \text{for } e=1,\dots,\mathtt{n_e}, \tag{35b}$$

where an arbitrary test function in the space $[\hat{\mathcal{V}}^0(\Gamma\cup\Gamma_N)]^{\mathtt{n_{sd}}}$ has been selected in Equation (35a).

Remark 3. Equation (33c) of the local problem coincides with the compatibility condition (35b) enforcing the divergence-free nature of the velocity field cell-by-cell. Following the strategy discussed for the first and second-order FCFV method,[10,21] this equation is omitted from the local problems and imposed solely in the global one since it involves only the global variable $\hat{\boldsymbol{u}}^h$.

The discrete FCFV local problems are obtained starting from the linear discretisation described in section 3.2 for the velocity $\boldsymbol{u}_e^h$, a constant cell-by-cell approximation of the pressure p_e^h, the mixed variable $\boldsymbol{L}_e^h$ and the mean pressure ρ_e^h and a constant face-by-face approximation of the hybrid velocity $\hat{\boldsymbol{u}}^h$. It follows that

$$\mathbf{L}_e = -|\Omega_e|^{-1}\sqrt{\nu}\mathbf{Z}_e - |\Omega_e|^{-1}\sqrt{\nu}\sum_{j\in\mathcal{B}_e}|\Gamma_{e,j}|\boldsymbol{n}_j\otimes\hat{\mathbf{u}}_j, \tag{36a}$$

$$\mathbf{u}_e = \tilde{\mathbf{M}}_e^{-1}\tilde{\mathbf{B}}_e + \tilde{\mathbf{M}}_e^{-1}\sum_{j\in\mathcal{B}_e}\tau_j\tilde{\mathbf{R}}_j\hat{\mathbf{u}}_j, \tag{36b}$$

$$\mathtt{p}_e = \rho_e, \tag{36c}$$

where

$$\mathbf{Z}_e := \sum_{j\in\mathcal{D}_e}|\Gamma_{e,j}|\boldsymbol{n}_j\otimes\boldsymbol{u}_{D,j} \quad \text{and} \quad \tilde{\mathbf{B}}_e := \tilde{\mathbf{F}}_e + \sum_{j\in\mathcal{D}_e}\tau_j\tilde{\mathbf{D}}_j. \tag{37}$$

It is worth noticing that Equations (36a) and (36c) are identical to the original second-order FCFV[21] and only Equation (36b) is affected by the change of basis discussed above. More precisely,

$$(\tilde{\mathbf{M}}_e)_{IJ} := \mathbf{I}_{\mathtt{n_{sd}}}\sum_{j=1}^{\mathtt{n_f^e}}(\tilde{p}_{e,j})_J\tau_j\int_{\Gamma_{e,j}}\tilde{N}_I d\Gamma, \quad (\tilde{\mathbf{F}}_e)_I := \int_{\Omega_e}\tilde{N}_I\boldsymbol{s}d\Omega, \tag{38}$$

$$(\tilde{\mathbf{D}}_j)_I := \boldsymbol{u}_{D,j}\int_{\Gamma_{e,j}}\tilde{N}_I d\Gamma, \quad (\tilde{\mathbf{R}}_j)_{IJ} := \mathbf{I}_{\mathtt{n_{sd}}}\int_{\Gamma_{e,j}}\tilde{N}_I d\Gamma. \tag{39}$$

The discrete FCFV global system is obtained by plugging the expressions (36) of $\mathbf{u}_e$, $\mathtt{p}_e$, and $\mathbf{L}_e$ into Equation (35), leading to

$$\begin{bmatrix}\hat{\mathbf{K}}_{\hat{u}\hat{u}} & \hat{\mathbf{K}}_{\hat{u}\rho}\\ \hat{\mathbf{K}}_{\hat{u}\rho}^T & \mathbf{0}_{\mathtt{n_e}}\end{bmatrix}\begin{Bmatrix}\hat{\mathbf{u}}\\ \boldsymbol{\rho}\end{Bmatrix} = \begin{Bmatrix}\hat{\mathbf{f}}_{\hat{u}}\\ \hat{\mathbf{f}}_{\rho}\end{Bmatrix}. \tag{40}$$

It is straightforward to observe that the matrix of problem (40) features a saddle-point structure with a symmetric block $\hat{\mathbf{K}}_{\hat{u}\hat{u}}$ in the top-left position, as classical in the approximation of incompressible Stokes equations. Both the

left- and right-hand sides of the linear system above are assembled by computing for $i,j \in \mathcal{B}_e$ the contributions of each cell as

$$(\hat{\mathbf{K}}_{\hat{u}\hat{u}})^e_{i,j} := |\Gamma_{e,i}| \left[\tau_i\tau_j \tilde{\mathbf{P}}_{e,i} \left(\tilde{\mathbf{M}}_e^{-1}\tilde{\mathbf{R}}_j\right) - \nu|\Omega_e|^{-1}|\Gamma_{e,j}|(\boldsymbol{n}_i \cdot \boldsymbol{n}_j)\mathbf{I}_{\mathrm{n_{sd}}} - \tau_i\delta_{ij}\mathbf{I}_{\mathrm{n_{sd}}}\right], \tag{41a}$$

$$(\hat{\mathbf{K}}_{\hat{u}\rho})^e_i := |\Gamma_{e,i}|\boldsymbol{n}_i, \tag{41b}$$

$$(\hat{\mathbf{f}}_{\hat{u}})^e_i := |\Gamma_{e,i}| \left(\nu|\Omega_e|^{-1}\boldsymbol{n}_i \cdot \mathbf{Z}_e - \tau_i\tilde{\mathbf{P}}_{e,i}\left(\tilde{\mathbf{M}}_e^{-1}\tilde{\mathbf{B}}_e\right) - \boldsymbol{t}_i\ \chi_{\mathcal{N}_e}(i)\right), \tag{41c}$$

$$(\hat{\mathrm{f}}_{\rho})^e := -\sum_{j\in D_e} |\Gamma_{e,j}|\boldsymbol{u}_{D,j} \cdot \boldsymbol{n}_j. \tag{41d}$$

The operator utilised to project the linear velocity in each cell on the space of constant functions on the face $\Gamma_{e,i}$ is defined via the matrix $\tilde{\mathbf{P}}_{e,i}$

$$\tilde{\mathbf{P}}_{e,i} := \begin{bmatrix} \tilde{\mathbf{p}}_{e,i}^T & \mathbf{0}_{1\times3} \\ \mathbf{0}_{1\times3} & \tilde{\mathbf{p}}_{e,i}^T \end{bmatrix} \tag{42}$$

in 2D and

$$\tilde{\mathbf{P}}_{e,i} := \begin{bmatrix} \tilde{\mathbf{p}}_{e,i}^T & \mathbf{0}_{1\times4} & \mathbf{0}_{1\times4} \\ \mathbf{0}_{1\times4} & \tilde{\mathbf{p}}_{e,i}^T & \mathbf{0}_{1\times4} \\ \mathbf{0}_{1\times4} & \mathbf{0}_{1\times4} & \tilde{\mathbf{p}}_{e,i}^T \end{bmatrix} \tag{43}$$

in 3D, $\tilde{\mathbf{p}}_{e,i}$ being the vector introduced in (28) for the projection in the scalar case.

3.5 | Computational aspects

The implementation of a FCFV method features three steps. First, a preprocess routine to compute all the cell quantities required by the method. Second, the computation, assembly and solution of a global problem on the mesh faces with the hybrid variable as unknown. Finally, the solution of $\mathrm{n_e}$ local problems to retrieve the primal and mixed variable in each cell.

The current implementation assumes that the stabilisation parameter is constant in the whole domain. Therefore, for the Poisson problem, the entries of the matrices $\tilde{\mathbf{m}}_e$ in Equation (26) and the vectors $\tilde{\mathbf{d}}_j$ and $\tilde{\mathbf{r}}_j$ in Equation (27) can be precomputed. Analogously, for the Stokes problem, the entries of the matrices $\tilde{\mathbf{M}}_e$ and $\tilde{\mathbf{R}}_j$ in Equations (38) and (39), respectively, and the vector $\tilde{\mathbf{D}}_j$ in Equation (39) can be precomputed. These terms only require the calculation of the integral of the new basis functions over a generic face of a cell. More precisely, for a generic face in two dimensions and for a triangular face in three dimensions, the integrals are given by

$$\int_{\Gamma_{e,j}} \tilde{N}_1 d\Gamma = |\Gamma_{e,j}|, \quad \text{and} \quad \int_{\Gamma_{e,j}} \tilde{N}_k d\Gamma = |\Gamma_{e,j}| \left(\overline{x}^{e,j}_{k-1} - \overline{x}^{e}_{k-1}\right), \quad \text{for } k = 2, \dots M. \tag{44}$$

For a generic quadrilateral face in three dimensions, analytical integration is only feasible for the first basis function, $\tilde{N}_1$, whereas for the remaining basis functions, $\tilde{N}_k$ for $k = 2,\dots M$, a numerical quadrature is employed.

Similarly, the entries of the vectors $\tilde{\mathbf{f}}_e$ and $\tilde{\mathbf{F}}_e$ in Equations (26) and (38), respectively, for the Poisson and Stokes problems, can be precomputed via an integral of the new basis functions over a generic cell. For a triangular or tetrahedral cell, such integral is given by

$$\int_{\Omega_e} \tilde{N}_1 d\Omega = |\Omega_e|, \quad \text{and} \quad \int_{\Omega_e} \tilde{N}_k d\Omega = 0, \quad \text{for } k = 2, \dots M, \tag{45}$$

whereas for other cell types, the integral is computed numerically. Hence, the computational cost of the preprocess routine to determine the terms in (26)-(27) and (38)-(39) is limited.

TABLE 1 Number of operations required to compute the elemental matrix and right-hand side of the Poisson problem by the first and second-order FCFV methods for different cell types

Method	Triangle	Quadrilateral	Tetrahedron	Hexahedron	Prism	Pyramid
First-order	126	212	252	534	380	380
Second-order	354	592	932	1962	1400	1400

Abbreviation: FCFV, face-centred finite volume.

TABLE 2 Number of operations required to compute the elemental matrix and right-hand side of the Stokes problem by the first and second-order FCFV methods for different cell types

Method	Triangle	Quadrilateral	Tetrahedron	Hexahedron	Prism	Pyramid
First-order	168	272	364	714	525	525
Second-order	2340	3900	21 424	44 988	32 135	32 135

Abbreviation: FCFV, face-centred finite volume.

The proposed second-order FCFV method requires the solution of a global system of equations with exactly the same number of unknowns and nonzero entries of the global matrix of the first-order FCFV proposed in References 10,20. This is because the second-order FCFV uses the same constant approximation space for the hybrid variable, which is the only variable featuring in the global systems of Equations (30) and (41), respectively, for the Poisson and Stokes problems.

The extra cost of the second-order FCFV compared with the first-order FCFV is due to the extra operations required to assemble the global system. Tables 1 and 2 detail the number of operations required to compute one elemental matrix and one elemental right-hand side vector for the Poisson and Stokes problems, respectively, for the proposed second-order FCFV method and the first-order FCFV method introduced in Reference 10. More precisely, Table 1 presents the cost of computing one elemental contribution of Equation (30) and one of equation 22 in Reference 10, whereas Table 2 compares the cost of building one elemental block of Equation (41) with one of equation 39 in Reference 10.

Although the second-order method requires more operations for a given spatial discretisation, the extra accuracy provided results in a more efficient method, when the computational cost required to achieve a given accuracy is considered. To quantify this gain, Figure 1 shows the relative error of the velocity field measured in the $\mathcal{L}_2(\Omega)$ norm as a function of the CPU time for the first and second-order methods using different cell types. The test case considered involves the solution of the Stokes equations, in two and three dimensions, for a problem described in the following section, where the analytical solution is known. The meshes employed are the same meshes used in the numerical examples of the following sections, Figures 2 and 3. The results show that to achieve a 1% error, the second-order method is almost one order of magnitude faster in two dimensions whereas in three dimensions the second-order method is more than four order of magnitude faster.

Finally, the solution of Equations (24) and (36) for the local Poisson and Stokes problems, respectively, relies on precomputed quantities and can be easily performed in parallel being such computation independent cell-by-cell.

4 | AN AUTOMATIC MESH ADAPTIVITY STRATEGY FOR THE SECOND-ORDER FCFV

In Reference 21, the authors devised an error indicator using the higher convergence rate of the second-order FCFV method with respect to the original first-order FCFV approach.[10,20] The main drawback of the proposed error indicator is the high computational cost that induces the solution of an extra global problem to estimate the error of a numerical solution.

This work proposes an error indicator that does not require the solution of an extra global problem. Instead, only a local computation cell-by-cell is required to devise an accurate and efficient indicator to drive mesh adaptivity. The error indicator proposed here is significantly cheaper because it exploits the solution of the global system already computed for the second-order FCFV method to solve an extra local problem cell-by-cell. Hence, its cost is negligible when compared with the cost of assembling and solving an extra global problem as discussed in Reference 21.

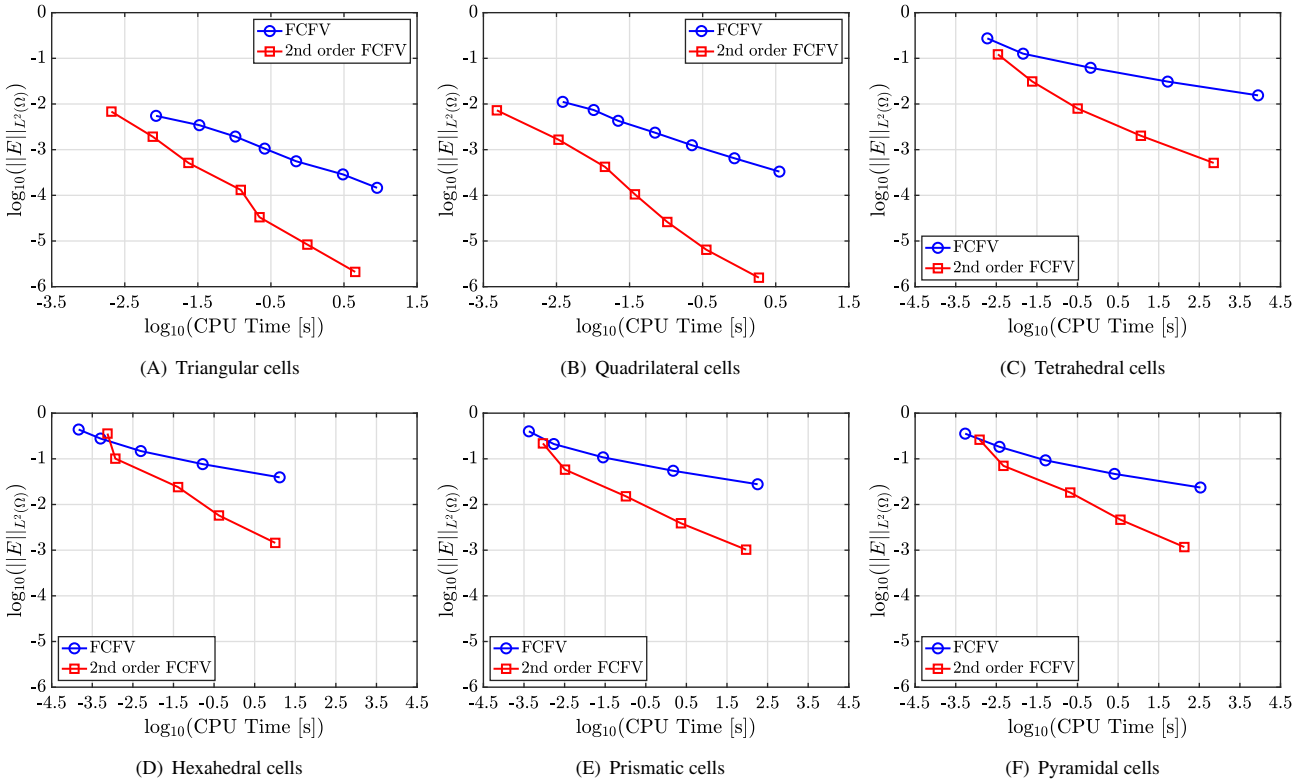

(A) Triangular cells (B) Quadrilateral cells (C) Tetrahedral cells

(D) Hexahedral cells (E) Prismatic cells (F) Pyramidal cells

FIGURE 1 Relative error of the velocity measured in the $\mathcal{L}_2(\Omega)$ norm as a function of the CPU time for the solution of the Stokes problem using, A, triangular, B, quadrilateral, C, tetrahedral, D, hexahedral, E, prismatic, and F, pyramidal cells [Colour figure can be viewed at wileyonlinelibrary.com]

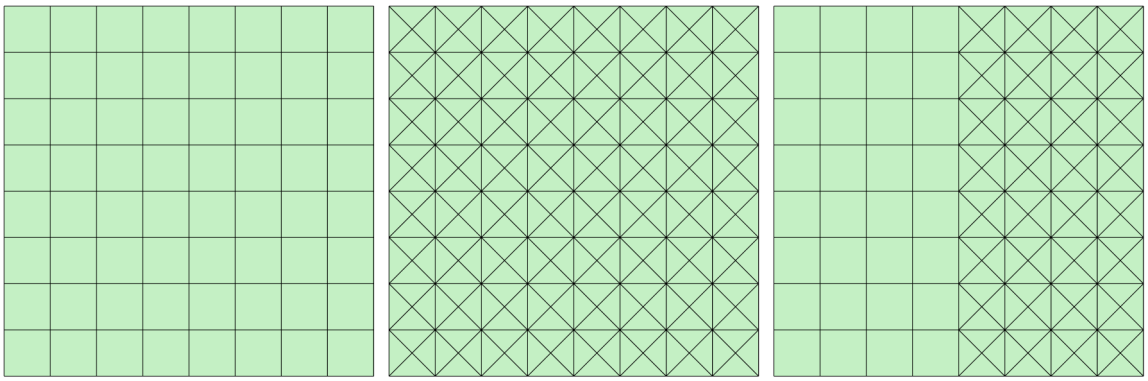

(A) Quadrilateral mesh (B) Triangular mesh (C) Hybrid mesh

FIGURE 2 Meshes corresponding to the third level of refinement for the domain $\Omega = [0,1]^2$ using, A, quadrilateral, B, triangular, and C, hybrid cells [Colour figure can be viewed at wileyonlinelibrary.com]

Hereafter, the proposed strategy is described for the Poisson problem but it is also applicable to the Stokes equations. After the global problem given by Equation (29) is solved, two approximations of the primal variable are computed using the same hybrid variable $\hat{u}$. On the one hand, a first approximation of the primal variable, u_e, is computed by solving the local, cell-by-cell, problem of Equation (24). On the other hand, a second approximation $u_e^\star$ is obtained by solving an extra local, cell-by-cell, problem corresponding to the first-order FCFV, first presented in Reference 10, namely

$$u_e^\star = \alpha_e^{-1}\beta_e + \alpha_e^{-1}\sum_{j\in\mathcal{B}_e}|\Gamma_{e,j}|\tau_j\hat{u}_j, \tag{46}$$

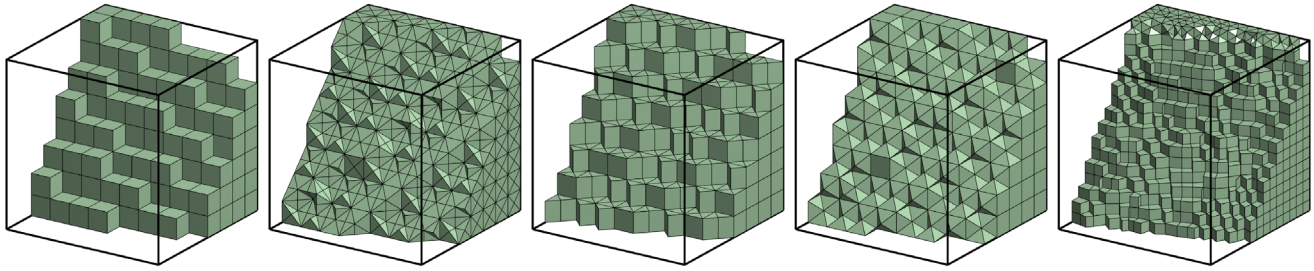

(A) Hexahedral mesh (B) Tetrahedral mesh (C) Prismatic mesh (D) Pyramidal mesh (E) Hybrid mesh

FIGURE 3 Internal view of the meshes corresponding to the fourth level of refinement for the domain $\Omega = [0,1]^3$ featuring, A, hexahedral, B, tetrahedral, C, prismatic, D, pyramidal, and E, hybrid cells [Colour figure can be viewed at wileyonlinelibrary.com]

where

$$\alpha_e := \sum_{j \in \mathcal{A}_e} |\Gamma_{e,j}| \tau_j, \quad \beta_e := |\Omega_e| s_e + \sum_{j \in D_e} |\Gamma_{e,j}| \tau_j u_{D,j}, \tag{47}$$

and $\mathcal{A}_e$ denotes the set of all faces of cell Ω_e.

The local error indicator for the cell Ω_e is thus defined as

$$E_e := \left[\frac{1}{|\Omega_e|} \int_{\Omega_e} \left(\mathrm{u}_e - \mathrm{u}_e^\star \right)^2 d\Omega \right]^{1/2}, \tag{48}$$

and it is employed to devise an automatic mesh adaptivity process. First, the following a priori local error estimate for elliptic problems is recalled[34-37]

$$\varepsilon_e := \| u^{\mathrm{ex}} - u^h \|_{\mathcal{L}_2(\Omega_e)} \leq C h_e^{1+\mathrm{n_{sd}}/2}, \tag{49}$$

where u^{ex} and u^h are the exact solution and its constant approximation in the cell Ω_e, respectively, h_e is the characteristic cell size and C is an unknown constant. Then, using a classical Richardson extrapolation, the desired cell size is calculated as

$$h_e^\star = h_e \left(\frac{\varepsilon}{E_e} \right)^{1/\left(1+\mathrm{n_{sd}}/2\right)}. \tag{50}$$

where ε is the user-defined target error in each cell. It is worth noting that the corresponding formula in Reference 21, namely, equation (47), presents a typo in the exponent of ε/E_e.

Remark 4. The accuracy of the error indicator (48) is guaranteed because u_e is a second-order approximation of the solution, whereas $\mathrm{u}_e^\star$ converges with first-order only. Moreover, this indicator provides information about the error between the solution $\mathrm{u}_e^\star$ and the exact solution but, as it will be shown in the numerical examples, it also provides information about the error between solution u_e and the exact solution.

To illustrate the efficiency of the proposed strategy, Table 3 reports the number of operations required by the error indicator in Reference 21 and by the new error indicator proposed in this work for the Poisson problem, and using different cell types. Similarly, Table 4 show the corresponding number of operations for the Stokes problem. The tables display the number of operations required in each case to compute the error indicator for a mesh of 1000 cells of different types. Concerning the indicator in Reference 21, its cost is given by the operations required to assemble and solve the extra global problem and to compute the corresponding u_e for each cell using the new hybrid variable. The strategy proposed here only involves the extra computation of Equation (46) for each cell. The results show that the new error indicator is several orders of magnitude less expensive. In addition, the number of operations of the proposed error indicator scales linearly with the number of cells, whereas the number of operations required by the error indicator proposed in Reference 21 scales with the cube of the number of cells, due to the required extra solution of a global linear system.

TABLE 3 Number of operations required to compute the error indicator of the Poisson problem for a mesh with 1000 cells of different types

Method	Triangle	Quadrilateral	Tetrahedron	Hexahedron	Prism	Pyramid
Error indicator in Reference 21	5.6×10^{8}	1.3×10^{9}	1.3×10^{9}	4.5×10^{9}	2.6×10^{9}	2.6×10^{9}
Error indicator (48)	1.0×10^{4}	1.3×10^{4}	1.3×10^{4}	1.9×10^{4}	1.6×10^{4}	1.6×10^{4}

TABLE 4 Number of operations required to compute the error indicator of the Stokes problem for a mesh with 1000 cells of different types

Method	Triangle	Quadrilateral	Tetrahedron	Hexahedron	Prism	Pyramid
Error indicator in Reference 21	1.1×10^{10}	2.1×10^{10}	5.7×10^{10}	1.7×10^{11}	1.0×10^{11}	1.0×10^{11}
Error indicator (48)	1.7×10^{4}	2.2×10^{4}	3.1×10^{4}	4.5×10^{4}	3.8×10^{4}	3.8×10^{4}

5 | NUMERICAL STUDIES

This section presents an extensive set of experiments to numerically validate the optimal convergence properties of the proposed method and to show its robustness against the choice of the stabilisation parameter and the mesh properties such as cell distortion and stretching. The examples presented involve meshes of different cell types, namely, triangular and quadrilateral cells in two dimensions, and tetrahedral, hexahedral, prismatic, and pyramidal cells in three dimensions. In addition, results with hybrid meshes are presented for the first time in the context of the FCFV method.

The model problem considered for the Poisson equation involves the numerical solution of (1) in $\Omega = [0,1]^{n_{sd}}$. In two dimensions, the source term and boundary data are selected such that the analytical solution is known and given by

$$u^{ex}(x_1,x_2) = \exp\left(\alpha\sin(ax_1+cx_2)+\beta\cos(bx_1+dx_2)\right), \tag{51}$$

with $\alpha=0.1$, $\beta=0.3$, $a=5.1$, $b=4.3$, $c=-6.2$, and $d=3.4$. Neumann boundary conditions are imposed on the bottom part of the boundary, on $\Gamma_N=\{(x_1,x_2)\in\mathbb{R}^2 \mid x_2=0\}$, and Dirichlet boundary conditions are set on the rest of the boundary. For the 3D Poisson problem, the source term and boundary data are selected such that the analytical solution is

$$u^{ex}(x_1,x_2,x_3) = \exp\left(\alpha\sin(ax_1+cx_2+ex_3)+\beta\cos(bx_1+dx_2+fx_3)\right), \tag{52}$$

with $\alpha=0.1$, $\beta=0.3$, $a=5.1$, $b=4.3$, $c=-6.2$, $d=3.4$, $e=1.8$, and $f=1.7$. Neumann boundary conditions are imposed on $\Gamma_N=\{(x_1,x_2,x_3)\in\mathbb{R}^3 \mid x_3=0\}$, whereas on the remaining boundary surfaces, Dirichlet conditions are enforced.

The domain $\Omega=[0,1]^{n_{sd}}$ is also utilised for the Stokes Equation (31) with viscosity $\nu=1$. For the 2D case, the source term and boundary conditions are devised in order for the analytical velocity and pressure fields to be

$$\begin{cases} u_1^{ex}(x_1,x_2) = x_1^2(1-x_1)^2(2x_2-6x_2^2+4x_2^3), \\ u_2^{ex}(x_1,x_2) = -x_2^2(1-x_2)^2(2x_1-6x_1^2+4x_1^3), \\ p^{ex}(x_1,x_2) = x_1(1-x_1). \end{cases} \tag{53}$$

On $\Gamma_N=\{(x_1,x_2)\in\mathbb{R}^2 \mid x_2=0\}$, a Neumann condition representing a pseudo-traction is imposed, whereas the analytical velocity enforcing Dirichlet conditions is set on the rest of the boundary. Similarly, in three dimensions, Neumann boundary conditions are imposed on $\Gamma_N=\{(x_1,x_2,x_3)\in\mathbb{R}^3 \mid x_3=0\}$ and Dirichlet conditions on the rest of the boundary, to match the analytical expressions of velocity and pressure given by

$$\begin{cases} u_1^{ex}(x_1,x_2,x_3) = \frac{1}{2}+(x_3-x_2)\sin\left(x_1-\frac{1}{2}\right), \\ u_2^{ex}(x_1,x_2,x_3) = 1-x_2\left(x_3-\frac{1}{2}x_2\right)\cos\left(x_1-\frac{1}{2}\right)-x_2\left(x_1-\frac{1}{2}x_2\right)\cos\left(x_3-\frac{1}{2}\right), \\ u_3^{ex}(x_1,x_2,x_3) = \frac{1}{2}+(x_1-x_2)\sin\left(x_3-\frac{1}{2}\right), \\ p^{ex}(x_1,x_2,x_3) = x_1(1-x_1)+x_2(1-x_2)+x_3(1-x_3). \end{cases} \tag{54}$$

TABLE 5 Details of the six hybrid meshes for the convergence study in three dimensions

Mesh	Number of cells	Hexahedral cells	Tetrahedral cells	Pyramidal cells	h
1	8	1	2	5	1.414
2	140	42	28	70	0.413
3	868	434	124	310	0.209
4	6226	4245	566	1415	0.104
5	20 340	15 594	1356	3390	0.071
6	64 638	53 865	3078	7695	0.047

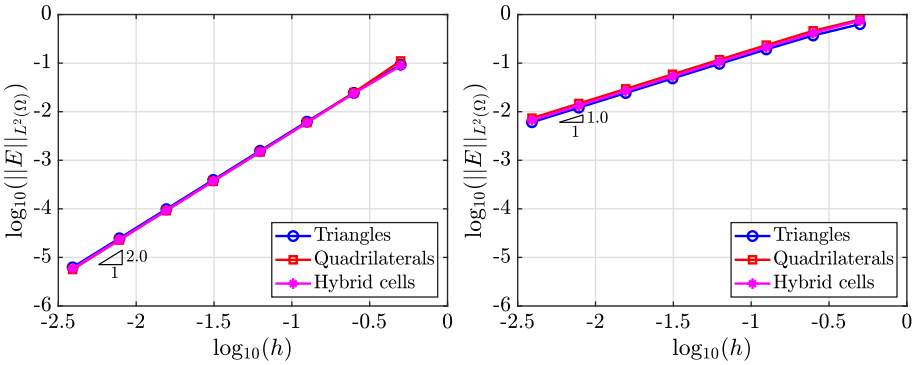

(A) u (B) $\boldsymbol{q}$

FIGURE 4 Mesh convergence of the error of the solution u and its gradient $\boldsymbol{q}$ in the $\mathcal{L}_2(\Omega)$ norm as a function of the cell size h for two-dimensional Poisson problem on regular meshes using different cell types [Colour figure can be viewed at wileyonlinelibrary.com]

To perform the mesh convergence study in two dimensions, a set of eight uniform triangular and quadrilateral meshes are generated. The meshes corresponding to the third level of refinement are displayed in Figure 2A,B. To demonstrate the flexibility of the proposed method, hybrid meshes made of quadrilateral and triangular cells are also considered. The third hybrid mesh is displayed in Figure 2C.

In three dimensions, a set of six uniforms tetrahedral, hexahedral, prismatic, and pyramidal meshes are generated. In addition, hybrid meshes containing a mixture of different cell types are also considered. Figure 3 shows the fourth level of mesh refinement for the different types of meshes considered and Table 5 shows the statistics for the hybrid meshes.

5.1 | Optimal convergence of the FCFV method

The first experiment involves a mesh convergence study for the Poisson and Stokes problems both in two and three dimensions and using meshes with different cell types. In all cases the stabilisation parameter is selected to be $\tau = 10^4$ in two dimensions and $\tau = 10^2$ for 3D problems. A detailed study of the influence of the stabilisation parameter on the accuracy of the proposed FCFV method is provided in section 5.2.

For the 2D Poisson problem, Figure 4 shows the relative error, measured in the $\mathcal{L}_2(\Omega)$ norm, of the primal and mixed variables as a function of the characteristic cell size. The results show optimal, quadratic, convergence of the primal variable for triangular, quadrilateral, and hybrid meshes with almost identical accuracy in the three cases. For the mixed variable an optimal, linear, convergence is also observed, again, with almost identical accuracy in the three cases.

The same mesh convergence study is performed for the 3D Poisson problem. Figure 5 shows the relative error of the primal and mixed variables, measured in the $\mathcal{L}_2(\Omega)$ norm, as a function of the characteristic cell size. The results display a similar qualitative behaviour when compared with the 2D case. An optimal, quadratic, convergence is observed for the primal variable and an optimal, linear, rate of convergence is observed for the mixed variable, for all cell types and hybrid meshes. Tetrahedral and hybrid meshes provide slightly more accurate results when compared with hexahedral, prismatic and pyramidal meshes.

Next, the mesh convergence study is performed for the Stokes problem in two and three dimensions. Figure 6 displays the relative error of velocity, pressure, and gradient of velocity, measured in the $\mathcal{L}_2(\Omega)$ norm, as a function of the characteristic cell size. The results show again an optimal quadratic convergence of the error of the velocity for all the different

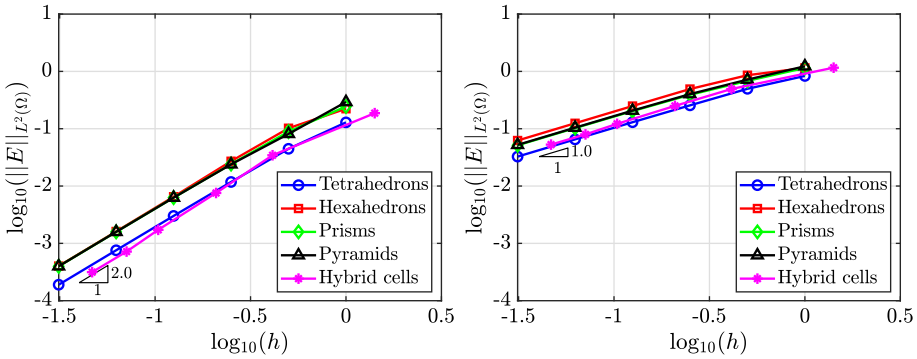

(A) u (B) q

FIGURE 5 Mesh convergence of the error of the solution u and its gradient $\boldsymbol{q}$ in the $\mathcal{L}_2(\Omega)$ norm as a function of the cell size h for three-dimensional Poisson problem on regular meshes using different cell types [Colour figure can be viewed at wileyonlinelibrary.com]

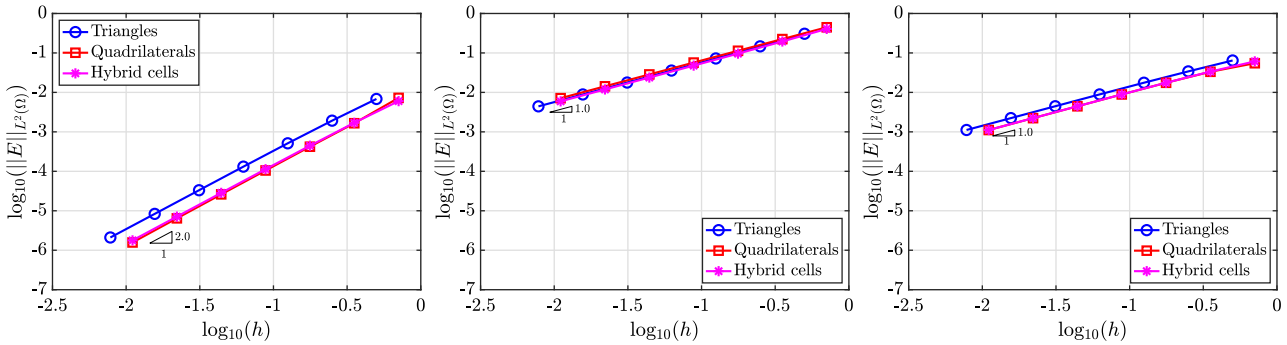

(A) $\boldsymbol{u}$ (B) p (C) $\boldsymbol{L}$

FIGURE 6 Mesh convergence of the error of velocity $\boldsymbol{u}$, pressure p, and gradient of velocity $\boldsymbol{L}$ in the $\mathcal{L}_2(\Omega)$ norm as a function of the cell size h for two-dimensional Stokes problem on regular meshes using different cell types [Colour figure can be viewed at wileyonlinelibrary.com]

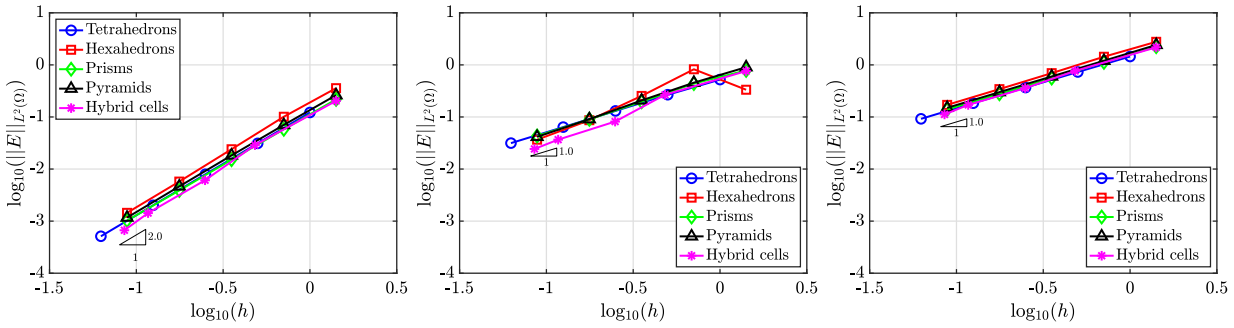

(A) $\boldsymbol{u}$ (B) p (C) $\boldsymbol{L}$

FIGURE 7 Mesh convergence of the error of velocity $\boldsymbol{u}$, pressure p, and gradient of velocity $\boldsymbol{L}$ in the $\mathcal{L}_2(\Omega)$ norm as a function of the cell size h for three-dimensional Stokes problem on regular meshes using different cell types [Colour figure can be viewed at wileyonlinelibrary.com]

types of meshes. For the pressure and the gradient of the velocity, optimal, linear, convergence of the error is also observed for all types of meshes. The same conclusions are observed from the results of the Stokes problem in three dimensions, displayed in Figure 7.

5.2 | Influence of the stabilisation parameter

The influence of the stabilisation parameter τ is studied numerically. The results in this section only consider the Stokes problem as further numerical examples, not reported here for brevity, have shown that identical conclusions are obtained

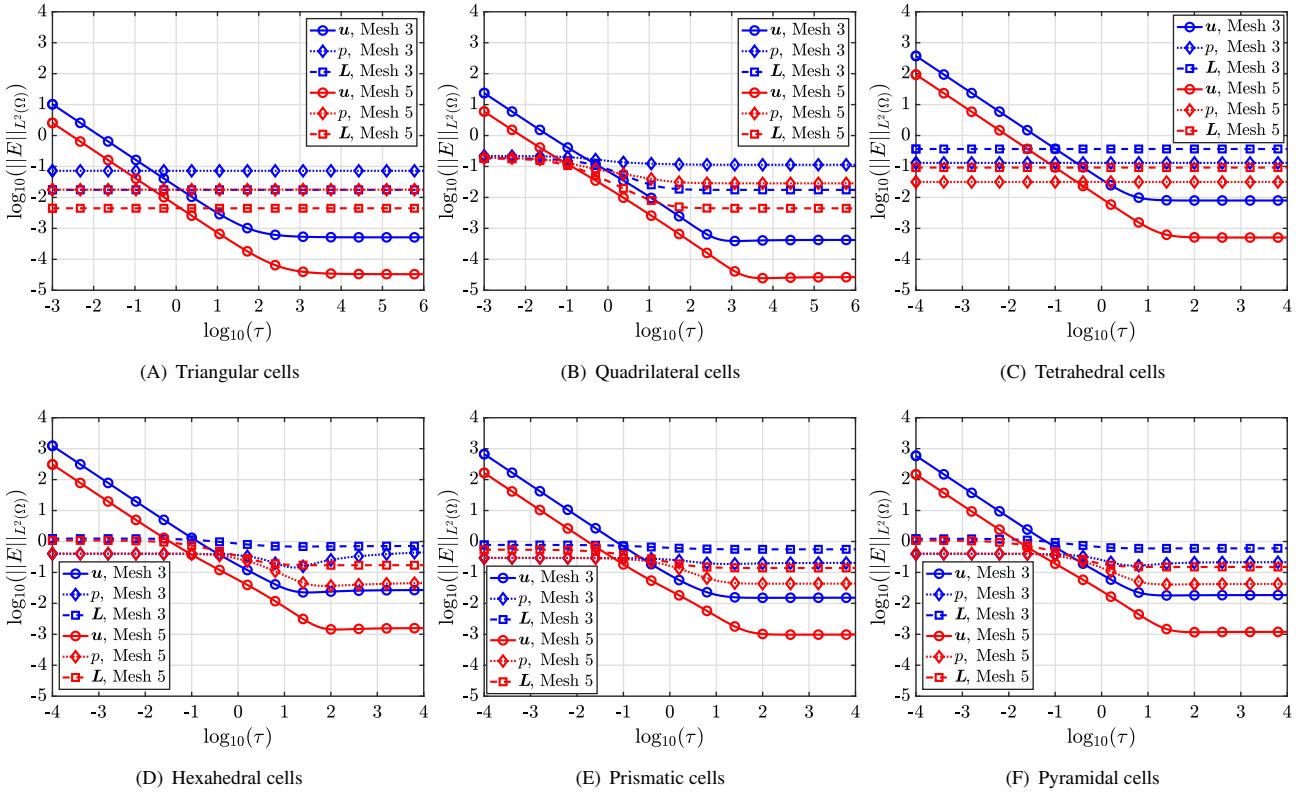

(A) Triangular cells (B) Quadrilateral cells (C) Tetrahedral cells

(D) Hexahedral cells (E) Prismatic cells (F) Pyramidal cells

FIGURE 8 Error of velocity $\boldsymbol{u}$, pressure p, and gradient of velocity $\boldsymbol{L}$ in the $\mathcal{L}_2(\Omega)$ norm as a function of the stabilisation parameter τ for the Stokes problem using, A, triangular, B, quadrilateral, C, tetrahedral, D, hexahedral, E, prismatic, and F, pyramidal cells [Colour figure can be viewed at wileyonlinelibrary.com]

for the Poisson problem. It is worth noting that the formulation presented in sections 3.3 and 3.4 for the Poisson and Stokes equations, respectively, enables the use of a different stabilisation parameter in each face.

Figure 8 shows the evolution of the relative error of velocity, pressure, and gradient of velocity in the $\mathcal{L}_2(\Omega)$ norm as a function of the stabilisation parameter τ. The results include two different levels of mesh refinement and different cell types in two and three dimensions. It is worth emphasising that the range of values of the stabilisation parameter utilised for the experiment in two dimensions is different to the range used in three dimensions.

Remark 5. For the Stokes equations, the usual definition of the stabilisation parameter is $\tau = \kappa\nu/\ell$, where ν is the viscosity of the fluid, ℓ is a characteristic length of the domain and κ is a constant scaling factor.[38] For the case under analysis, it holds $\nu = 1$ and $\ell = 1$, the domain being the unit square and the unit cube in two and three dimensions, respectively. Hence, Figure 8 is obtained by varying the value of the scaling factor κ in the definition of the stabilisation parameter above. It is worth noting that for convection-diffusion problems, not considered here, two different stabilisation parameters are employed. The stabilisation parameter associated to the diffusion operator is defined as in this work, whereas a different stabilisation is introduced for the convection operator.[38]

In all cases, the results show that a low value of the stabilisation parameter leads to a high error for the primal variable, whereas a large value, namely, $\tau = 10^4$ in two dimensions and $\tau = 10^2$ in three dimensions, provides the maximum accuracy for the velocity. When triangular or tetrahedral cells are considered, the error of the gradient of the velocity and the pressure is found to be independent on the value of the stabilisation parameter used. By contrast, for quadrilateral and hexahedral cells, the error of the gradient of the velocity and the pressure decreases as the value of τ increases. For these cell types, the maximum accuracy is reached for a value of $\tau = 10^4$ in two dimensions and $\tau = 10^2$ in three dimensions. Finally, for prismatic and pyramidal cells, the accuracy of the gradient of the velocity and the pressure is less sensitive to the choice of τ and the qualitative behaviour is extremely similar to the one observed for quadrilateral and hexahedral cells.

Henceforth, the stabilisation parameter is selected as $\tau = 10^4$ in two dimensions and $\tau = 10^2$ in three dimensions, for both Poisson and Stokes problems and for any cell type.

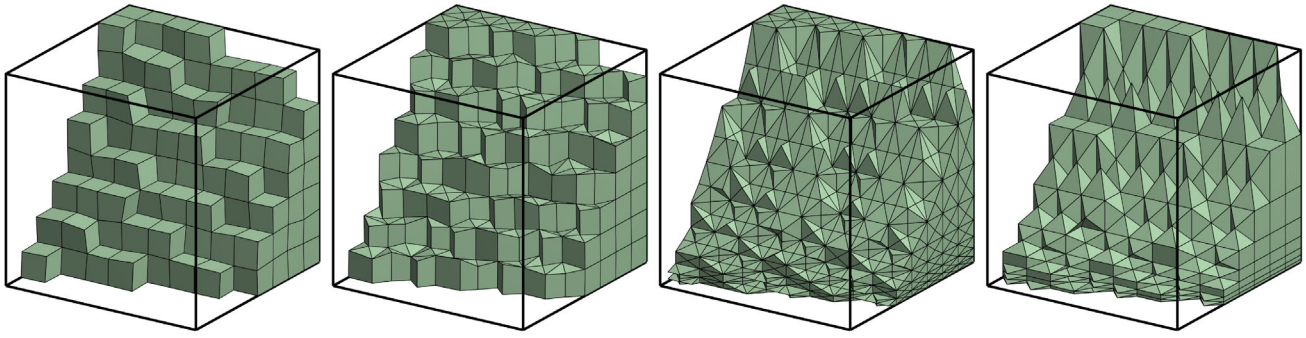

(A) Distored hexahedrons (B) Distored prisms (C) Stretched tetrahedrons (D) Stretched pyramids

FIGURE 9 Internal view of the meshes corresponding to the fourth level of refinement for the domain $\Omega = [0,1]^3$ featuring, A, distorted hexahedral, B, distorted prismatic, C, stretched tetrahedral, and D, stretched pyramidal cells [Colour figure can be viewed at wileyonlinelibrary.com]

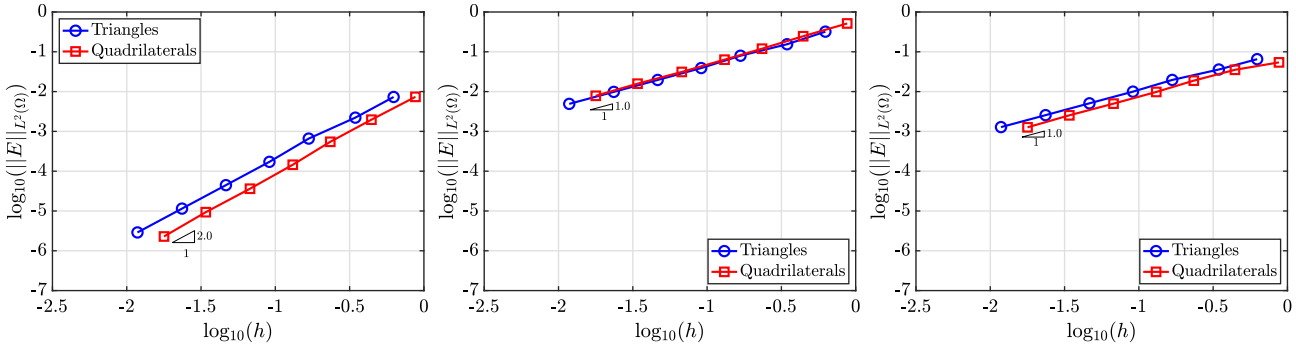

(A) $\boldsymbol{u}$ (B) p (C) $\boldsymbol{L}$

FIGURE 10 Mesh convergence of the error of velocity $\boldsymbol{u}$, pressure p, and gradient of velocity $\boldsymbol{L}$ in the $\mathcal{L}_2(\Omega)$ norm as a function of the mesh size h for two-dimensional Stokes problem using meshes of distorted cells [Colour figure can be viewed at wileyonlinelibrary.com]

5.3 | Influence of cell distortion and stretching

Previous experiments, employed to test the optimal approximation properties of the proposed method, involved regular meshes. In this section, the effect of cell distortion and stretching on the accuracy of the proposed method is studied. This is of major importance for the method to be applicable to more complicated problems involving complex geometries and for its extension to computational fluid dynamics applications involving boundary layers.

Cell distortion is introduced by perturbing the internal nodes of the mesh according to a random variation of maximum magnitude $h_{\min}/4$, where $h_{\min}$ is the minimum edge of the regular mesh. For cells with quadrilateral faces, the motion is constrained to ensure that all faces on the distorted mesh are planar.[39] Figure 9A,B show two examples of distorted meshes for hexahedral and prismatic cells. Similarly, cell stretching is introduced by transforming the regular meshes employed in previous experiments. The stretching factor, s, is measured as the ratio between the maximum and minimum faces/edges in a cell. Figure 9C,D show two examples of stretched meshes for tetrahedral and pyramidal cells for $s = 10$.

The mesh convergence results for the Stokes problem in two and three dimensions using meshes with distorted cells are shown in Figures 10 and 11, respectively. In two dimensions, the optimal convergence properties are observed for velocity, pressure, and gradient of velocity both using triangular and quadrilateral meshes. Furthermore, it can be observed that, for the same level of mesh refinement, quadrilateral cells provide more accurate results when compared with meshes with triangular cells. Similar conclusions are obtained in three dimensions, where optimal rate of convergence is achieved in all cases for velocity, pressure, and gradient of velocity and comparable accuracy is provided by all cell types.

The convergence study on stretched meshes with stretching factor $s = 10$ and $s = 100$, is performed for the Poisson problem. Figure 12 shows the relative error, measured in the $\mathcal{L}_2(\Omega)$ norm, of the primal and mixed variables as a

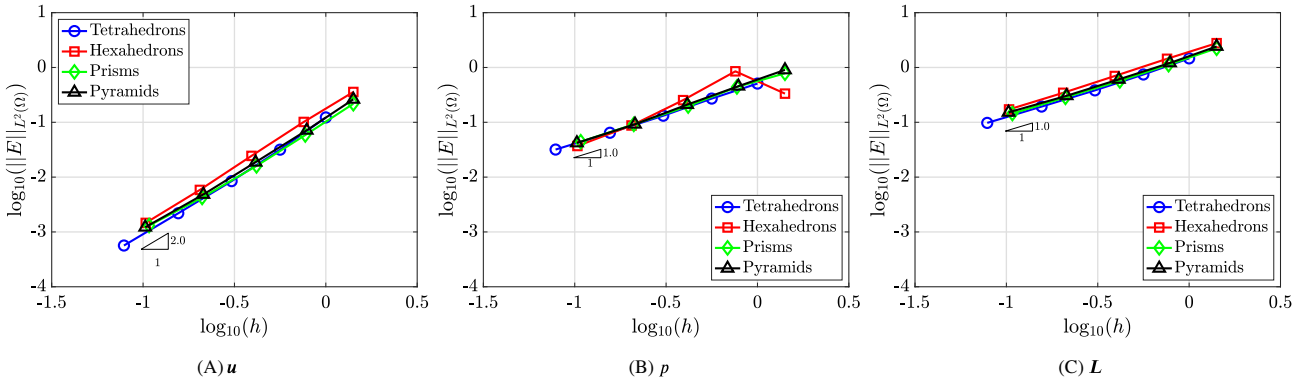

(A) $\boldsymbol{u}$ (B) p (C) $\boldsymbol{L}$

FIGURE 11 Mesh convergence of the error of velocity $\boldsymbol{u}$, pressure p, and gradient of velocity $\boldsymbol{L}$ in the $\mathcal{L}_2(\Omega)$ norm as a function of the mesh size h for three-dimensional Stokes problem using meshes of distorted cells [Colour figure can be viewed at wileyonlinelibrary.com]

FIGURE 12 Mesh convergence of the error of the solution u and its gradient $\boldsymbol{q}$ in the $\mathcal{L}_2(\Omega)$ norm for the two-dimensional Poisson problem using meshes of stretched cells, with maximum stretching factor $s = 10$ and $s = 100$ [Colour figure can be viewed at wileyonlinelibrary.com]

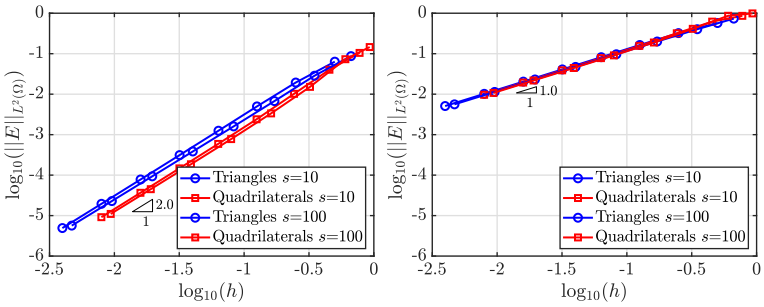

(A) u (B) $\boldsymbol{q}$

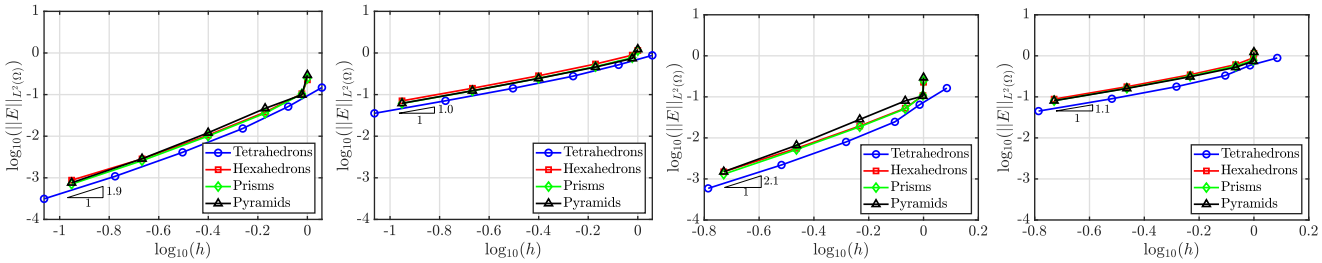

(A) u, $s = 10$ (B) $\boldsymbol{q}$, $s = 10$ (C) u, $s = 100$ (D) $\boldsymbol{q}$, $s = 100$

FIGURE 13 Mesh convergence of the error of the solution u and its gradient $\boldsymbol{q}$ in the $\mathcal{L}_2(\Omega)$ norm for the three-dimensional Poisson problem using meshes of stretched cells, with maximum stretching factor $s = 10$ and $s = 100$ [Colour figure can be viewed at wileyonlinelibrary.com]

function of the characteristic cell size. The results reveal that the accuracy of the proposed method is not dependent on the stretching factor. The conclusions also hold for the Poisson problem in three dimensions, as illustrated by the results in Figure 13. Optimal convergence is observed for all the variables and all cell types. The accuracy is again found to be almost insensitive to the stretching factor.

Further numerical experiments, not reported here for brevity, demonstrated that the same conclusions are obtained when performing the numerical experiments for the Poisson problem on meshes with distorted cells and the Stokes problem on meshes with stretched cells.

5.4 | Computational cost

The last numerical experiment involves a study of the computational cost of the proposed method for meshes with different cell types. The computational efficiency is compared by directly measuring the CPU time

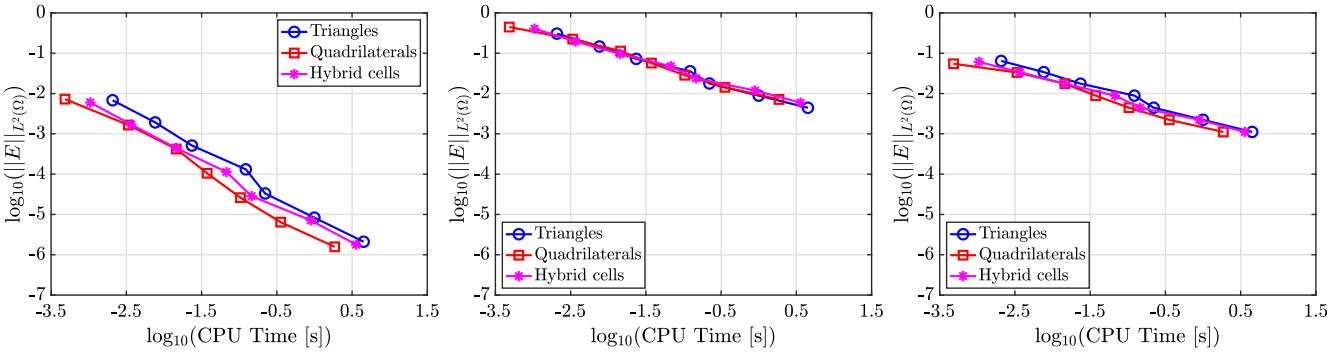

(A) $\boldsymbol{u}$ (B) p (C) $\boldsymbol{L}$

FIGURE 14 Error of velocity $\boldsymbol{u}$, pressure p, and gradient of velocity $\boldsymbol{L}$ in the $\mathcal{L}_2(\Omega)$ norm as a function of the CPU time for two-dimensional Stokes problem using meshes of different cell types [Colour figure can be viewed at wileyonlinelibrary.com]

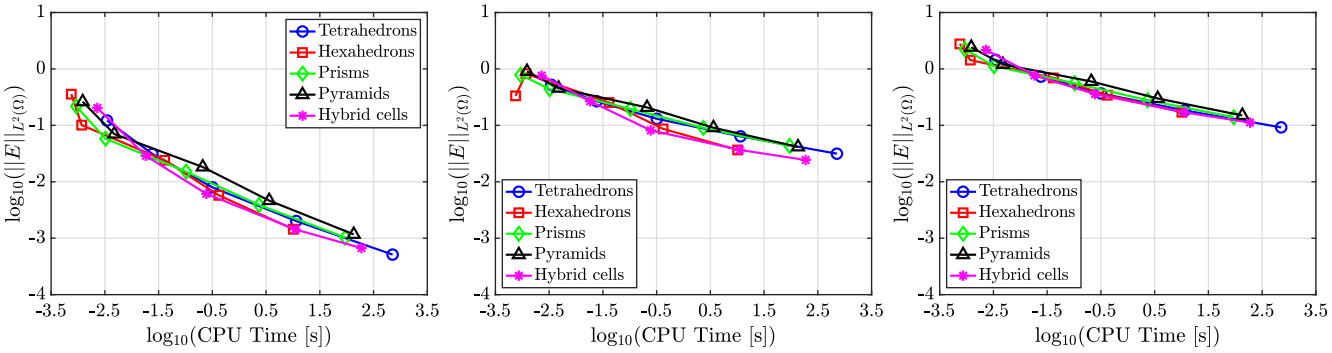

(A) $\boldsymbol{u}$ (B) p (C) $\boldsymbol{L}$

FIGURE 15 Error of velocity $\boldsymbol{u}$, pressure p, and gradient of velocity $\boldsymbol{L}$ in the $\mathcal{L}_2(\Omega)$ norm as a function of the CPU time for three-dimensional Stokes problem using meshes of different cell types [Colour figure can be viewed at wileyonlinelibrary.com]

(in seconds) required to assemble and solve the global system of equations, as this is the dominant cost of the proposed methodology.

Figure 14 displays the evolution of the relative error of velocity, pressure, and gradient of velocity in the $\mathcal{L}_2(\Omega)$ norm, as a function of the CPU time. The results reveal that quadrilateral and hybrid meshes provide the same accuracy as triangular meshes with slightly less computational effort. The better performance of quadrilateral cells is clearly observed when measuring the error of the velocity, whereas for pressure and gradient of velocity, all types of cells provide the same accuracy with a similar computational effort. It is worth noting that the advantages of using quadrilateral cells are not only observed when high accuracy is required. Even for an accuracy of 1% quadrilateral cells require nearly one order of magnitude less CPU time than triangles.

In three dimensions the conclusions are similar, as shown in Figure 15. Hexahedral and hybrid meshes are able to provide the solution with a given accuracy with slightly less computational effort when compared with tetrahedral, prismatic, and pyramidal meshes. The most important differences are appreciated when the error of the velocity is considered.

It is worth noting that quadrilateral and hexahedral meshes seem to provide the maximum performance, in terms of achieving the desired accuracy with the minimum computational effort. However, it is well known that the mesh generation of complex objects using unstructured hexahedral meshes is still today an open problem.[40] In this scenario, the ability of the proposed method to handle hybrid meshes will be of use. As demonstrated by the results of Figures 14 and 15, the use of hybrid meshes is still beneficial when compared with pure triangular or tetrahedral meshes.

6 | APPLICATIONS OF THE AUTOMATIC MESH ADAPTIVITY STRATEGY

This section presents two numerical examples solved with the proposed second-order FCFV in a mesh adaptivity framework. The first example involves the solution of a Poisson problem with known analytical solution on a simple 2D domain. This example is used to evaluate the performance of the error indicator introduced in Section 4. The second example involves the solution of the Stokes equations in a complex domain of interest for microfluidics applications[41,42] and it is used to demonstrate the potential of the proposed methodology.

In both examples an initial mesh is generated, assuming no previous knowledge of the solution. The global system is solved to obtain the approximation of the solution on the cell faces and two sets of local problems are solved to obtain the first and second-order approximations of the solution in the cells. Using the error indicator devised in Section 4, a desired cell size is defined in each cell. This information is used to build a background mesh that is employed to generate the mesh of the next adaptivity iteration.[43] The process is finished once the error indicator in all cells is below a user-defined tolerance.

6.1 | 2D heat transfer problem with localised source

The model problem (1) in $\Omega = [0,1]^2$ is considered, where the source term and boundary data are selected such that the analytical solution is known and given by

$$u^{\text{ex}}(x_1, x_2) = 1 + \exp\left\{-a\left((x_1 - b)^2 + (x_2 - b)^2\right)\right\}, \tag{55}$$

with $a = 100$ and $b = 0.7$. The variation of the solution is confined to a small region in the domain, around the point (0.7,0.7), due to the localised source term selected. This example is used to check the performance of the mesh adaptive process described in Section 4 and to highlight the capability of the error indicator (48) to identify the region of interest in the domain, where the variation of the solution is localised.

Two mesh adaptive simulations are performed, with triangular and quadrilateral meshes and imposing a desired error in each cell of $\epsilon = 10^{-2}$. The initial coarse triangular and quadrilateral meshes, shown in Figure 16A,D, have 128 and 16 cells, respectively. The first-order solutions, $u^\star$, computed with the initial coarse meshes, are shown in Figure 17A,G and the second-order solutions are displayed in Figure 17B,H.

After computing the error indicator, as detailed in Section 4, a desired size is determined for each cell of the coarse mesh. With this information, new meshes are generated, the first and second-order solutions are recomputed and the

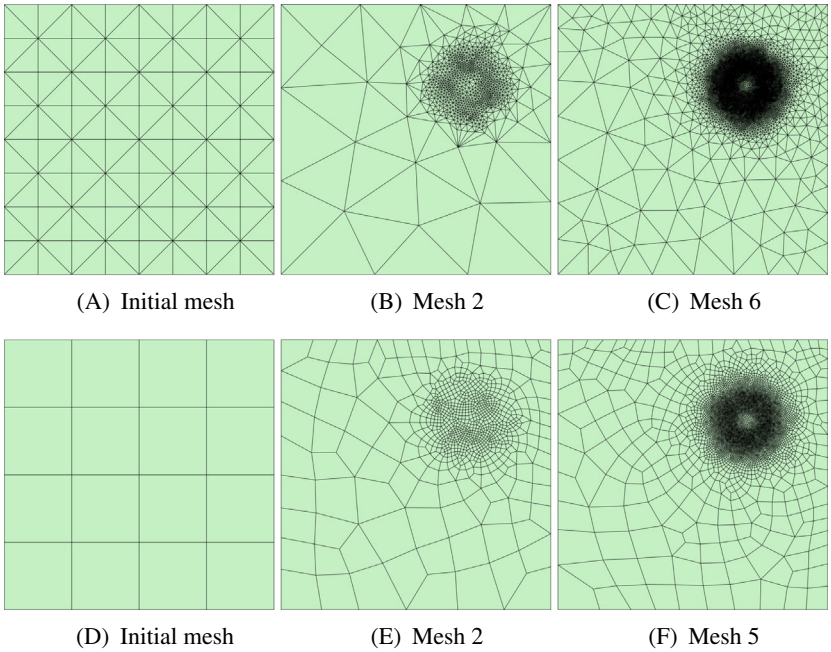

(A) Initial mesh (B) Mesh 2 (C) Mesh 6

(D) Initial mesh (E) Mesh 2 (F) Mesh 5

FIGURE 16 Initial (left), intermediate (middle), and final (right) meshes generated by the automatic mesh adaptive procedure with a tolerance $\epsilon = 10^{-2}$ for the Poisson problem using triangular (top) and quadrilateral (bottom) cells [Colour figure can be viewed at wileyonlinelibrary.com]

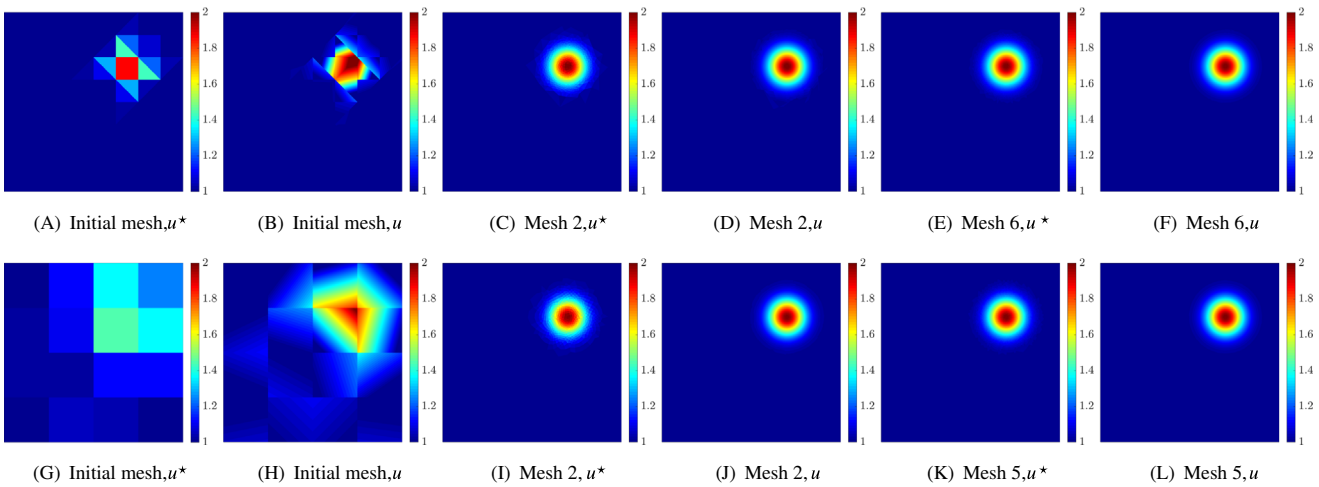

FIGURE 17 Initial, intermediate and final FCFV first-order, $u^\star$, and second-order, u, approximations for the Poisson problem using triangular (top) and quadrilateral (bottom) meshes depicted in Figure 16. FCFV, face-centred finite volume [Colour figure can be viewed at wileyonlinelibrary.com]

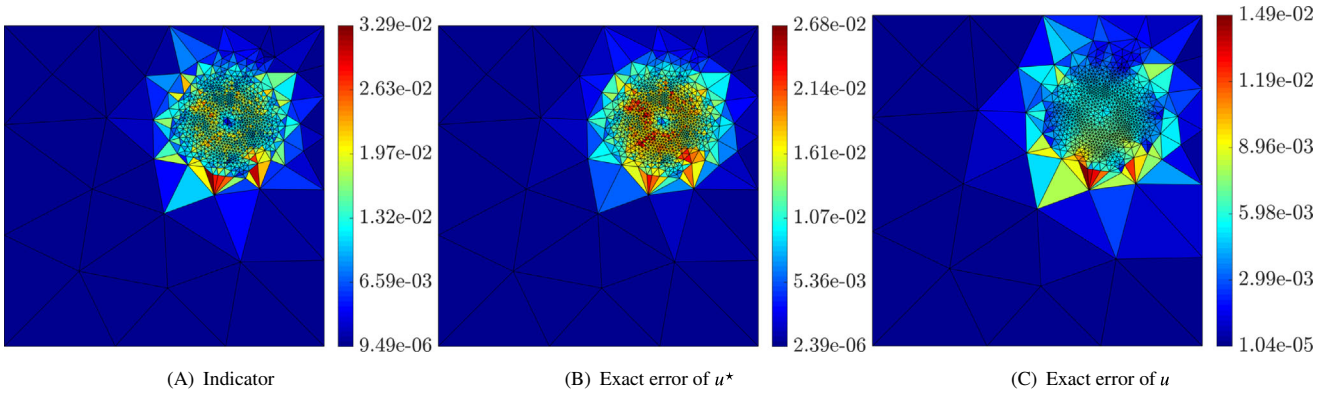

FIGURE 18 Comparison of A, error indicator, B, exact error of $u^\star$, and C, exact error of u on the second adapted triangular mesh [Colour figure can be viewed at wileyonlinelibrary.com]

mesh adaptivity procedure is repeated. Figure 16B,E display the meshes after two adaptivity iterations. The triangular mesh has 1755 cells, whereas the quadrilateral mesh has 895 cells. As it can be observed, the approximations computed at the second iteration of the mesh adaptive process already capture the main feature of the solution, which is a Gaussian profile centred at (0.7,0.7). The adaptive process converges in six iterations for triangular meshes and five iterations for quadrilateral meshes. The triangular and quadrilateral final meshes, shown in Figure 16C,F, have 17 821 and 9483 cells, respectively.

It is worth noticing that, away from the centre of the Gaussian hill, the meshes are refined more than the error indicator requires. This is automatically done by the mesh generator to ensure a smooth transition of the element size and guarantee a higher mesh quality. Despite previous numerical examples show that the FCFV is capable of producing accurate solutions irrespective of the mesh quality, traditional mesh generators tend to favour quality over the required element size.

Figure 18 displays a map of the error indicator (48) and of the exact errors of $u^\star$ and u on the second adapted triangular mesh. The indicator provides an accurate approximation of the error distribution of $u^\star$, only slightly overestimating it as detailed below in Figure 19C. In addition, the indicator shows good qualitative agreement with the exact error of the second-order FCFV approximation in Figure 18C.

Figure 18 also confirms that the error indicator correctly identifies that the south-west corner of the domain, where the solution is smooth, does not require additional refinement, which is nonetheless performed by the mesh generator.

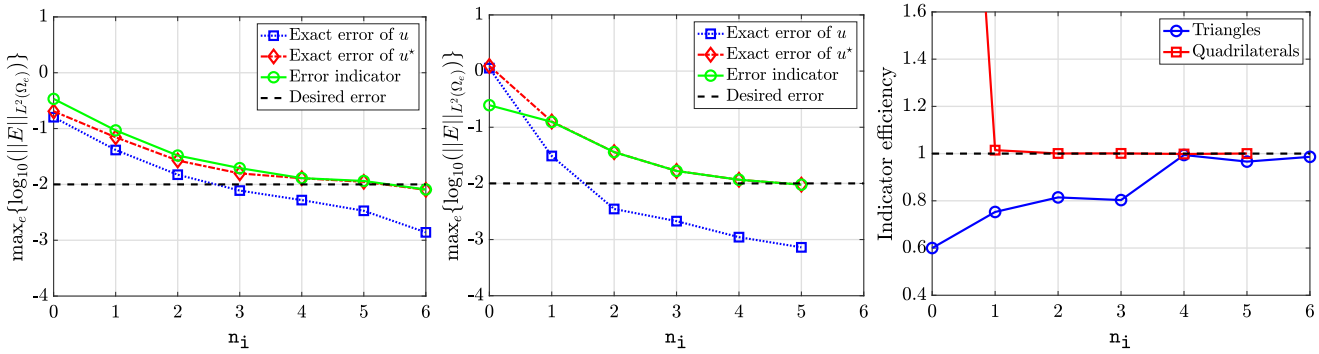

(A) Triangles (B) Quadrilaterals (C) Indicator efficiency

FIGURE 19 Maximum values of the error indicator and the exact error over all the cells as a function of the number of iterations of the mesh adaptive procedure using, A, triangular, B, quadrilateral cells, C, Indicator efficiency using triangular and quadrilateral meshes [Colour figure can be viewed at wileyonlinelibrary.com]

To further analyse these results, Figure 19A,B show the evolution of the maximum values of the error indicator and the exact error over all the cells as a function of the number of iterations of the mesh adaptive procedure, $\mathtt{n_i}$, for triangular and quadrilateral meshes, respectively. The results clearly show that the error indicator devised in Section 4 produces a very accurate estimate of the error of the approximation $u^\star$, computed by solving an inexpensive extra local problem given by Equation (46), for both types of meshes. A slight difference is observed between the error indicator and the exact error of $u^\star$ for triangular meshes for the first three iterations of the mesh adaptivity process, whereas for quadrilateral cells a perfect agreement is observed.

To quantify this difference, the so-called *indicator efficiency*, computed as the ratio between the exact error of $u^\star$ and the error indicator (48), is reported in Figure 19C. On the first iteration, the efficiency for triangular meshes is 0.75 and slowly improves during the adaptive process, being 0.8 in the third iteration, 0.97 in the fifth iteration and 0.99 in the final iteration. For quadrilateral cells, the indicator efficiency is already 1.01 in the first iteration and takes a value of 1.00 from the second to the fifth iteration.

This clearly indicates that in this example, the use of quadrilateral meshes is beneficial compared with triangular meshes. Not only less iterations of the mesh adaptivity process are required but, in addition, the final mesh is coarser and the error of the approximate solution is lower when using quadrilateral cells.

It is worth noting that despite the mesh adaptivity process is driven by computing an error indicator for the approximate solution $u^\star$, the error of the more accurate approximation u also decreases monotonically during the adaptive process, as shown in Figure 19A,B. This is expected due to the higher accuracy of the approximation computed with the proposed second-order FCFV, when compared with the accuracy of the first-order solution obtained by solving the extra local problem of Equation (46). The difference in accuracy can be observed in Figure 1, where the error of the first and second-order FCFV is compared for a Stokes problem in two and three dimensions. More precisely, from numerical experiments, it has been observed that the error of the approximation u is up to one order of magnitude lower than the error of $u^\star$. Since the error of $u^\star$ is utilised to drive adaptivity, this guarantees that the second-order FCFV approximation fulfils the required tolerance ε when the overall procedure stops. This extra accuracy, which may be interpreted as a safety factor, has been empirically estimated from numerical experiments in a factor between 0.1 and 0.5.

6.2 | 3D Stokes flow around complex microswimmers

The last example considers the 3D Stokes flow around microswimmers. The geometry of the microswimmers, taken from Reference 42, is given in parametric form as

$$\boldsymbol{S}(\lambda,\theta) = \boldsymbol{C}(\lambda) + R_n(\lambda)\sin(\theta)\boldsymbol{n}_1 + R_b(\lambda)\cos(\theta)\boldsymbol{n}_2, \quad (\lambda,\theta) \in [-L,L]\times[0,2\pi), \tag{56}$$

where the curve $\boldsymbol{C}$ is a parameterisation of the centreline of the swimmer, namely

$$\boldsymbol{C}(\lambda) = (\beta\cos(\kappa\lambda), \beta\sin(\kappa\lambda), \alpha\lambda)\,. \tag{57}$$

TABLE 6 Parameters used to define the geometry of the microswimmers

L	A_b	C_1	C_2	α	β	κ	λ_0	λ_1	σ
1	$L/27$	1.75	2.75	0.7	$(1-\alpha^2)^{1/2}/\kappa$	$4\pi/L$	$(1-9/54.2)L$	$(1-11/54.2)L$	$0.02L$

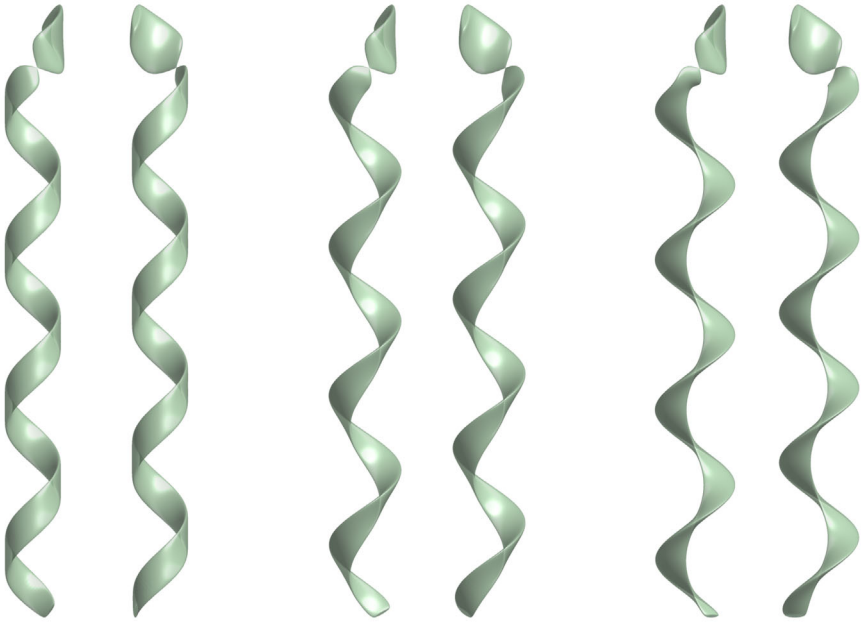

(A) $\gamma = 0$ (B) $\gamma = \pi/4$ (C) $\gamma = \pi/2$

FIGURE 20 Geometry of three microswimmers for the parameters given in Table 6, showing two perspectives of the same geometry [Colour figure can be viewed at wileyonlinelibrary.com]

In (56), $\boldsymbol{n}_1$ and $\boldsymbol{n}_2$ denote the unit normal vectors to the centreline tangent and serve as the short and long axis, respectively, of the propeller cross-section. More precisely, they are defined as

$$\boldsymbol{n}_1 = \cos(\gamma F_1(\lambda))\,\boldsymbol{N} + \sin(\gamma F_1(\lambda))\,\boldsymbol{B}, \quad \boldsymbol{n}_2 = \cos(\gamma F_1(\lambda))\,\boldsymbol{B} - \sin(\gamma F_1(\lambda))\,\boldsymbol{N}, \tag{58}$$

in terms of the Serret-Frenet normal $\boldsymbol{N}$ and bi-normal $\boldsymbol{B}$. The radii of the long and short axis of the propeller cross-sections of the swimmer, denoted by R_b and R_n, respectively, are defined as

$$R_b(\lambda) = A_b\,(C_1 + C_2 F_0(\lambda))\left(1-\lambda^8\right)^{1/8}, \quad R_n(\lambda) = \frac{1}{4}R_b(\lambda), \tag{59}$$

where the function F_s is defined, for $s = \{0,1\}$, as

$$F_s(\lambda) = \frac{1}{2}\left[1 - \operatorname{erf}\left(\frac{\lambda-\lambda_s}{\sqrt{2}\sigma}\right)\right]. \tag{60}$$

All the parameters appearing in the previous expressions are given in Table 6.

Three microswimmers, obtained by varying the parameter γ in Equation (58), are considered to demonstrate the potential of the automatic mesh adaptivity framework proposed in Section 4. The geometries of the three cases considered are displayed in Figure 20.

To perform the Stokes flow simulation, the microswimmers of volume $\mathcal{S}_\gamma$ are placed in the centre of a prismatic channel $\mathcal{B} = [-L_1, L_1] \times [-L_2, L_2] \times [-L_3, L_3]$, with $L_1 = L_2 = 17.14\,\mu\text{m}$ and $L_3 = 2L_1$. The resulting computational domain is given by $\Omega_\gamma = \mathcal{B} \backslash \mathcal{S}_\gamma$. A paraboloid velocity profile $\boldsymbol{u}_D(x_1, x_2, x_3) = (0, 0, -4.1(L_1^2 - x_1^2)(L_2^2 - x_2^2)/L_1^2 L_2^2)\mu\text{m/s}$ is imposed on the inlet, at $x_3 = L_3$, and a free-traction condition is enforced on the outlet, at $x_3 = -L_3$. On the remaining lateral walls of $\mathcal{B}$ and on the surface of the microswimmer, a no-slip boundary condition, corresponding to

material walls, is enforced. The kinematic viscosity is taken as $\nu = 2.65\,\text{mm}^2/\text{s}$, which is the value corresponding to blood at 37°C.

The initial meshes displayed in Figure 21 are generated, using the technique described in Reference 43, to start the automatic adaptivity process. To ensure a good geometric representation, the initial meshes are generated by imposing a desired cell size of 0.04 μm along the curves $\boldsymbol{S}(\lambda,0)$ and $\boldsymbol{S}(\lambda,\pi)$, for $\lambda\in[-L,L]$. The desired cell size in the rest of the domain is 0.5 μm. The resulting meshes have (a) 80 024, (b) 80 294, and (c) 77 533 cells for $\gamma = 0$, $\gamma = \pi/4$, and $\gamma = \pi/2$, respectively. It is worth noting that, due to the complexity of the geometry, only tetrahedral meshes are considered in this example.

The automatic mesh adaptive process is launched with a desired relative error of $\varepsilon = 5\times10^{-2}$. Convergence of the adaptivity procedure is achieved in five iterations for the three geometries considered. For the geometry corresponding to $\gamma = \pi/4$, Figure 22 shows the third, fourth and fifth mesh obtained during the automatic adaptive

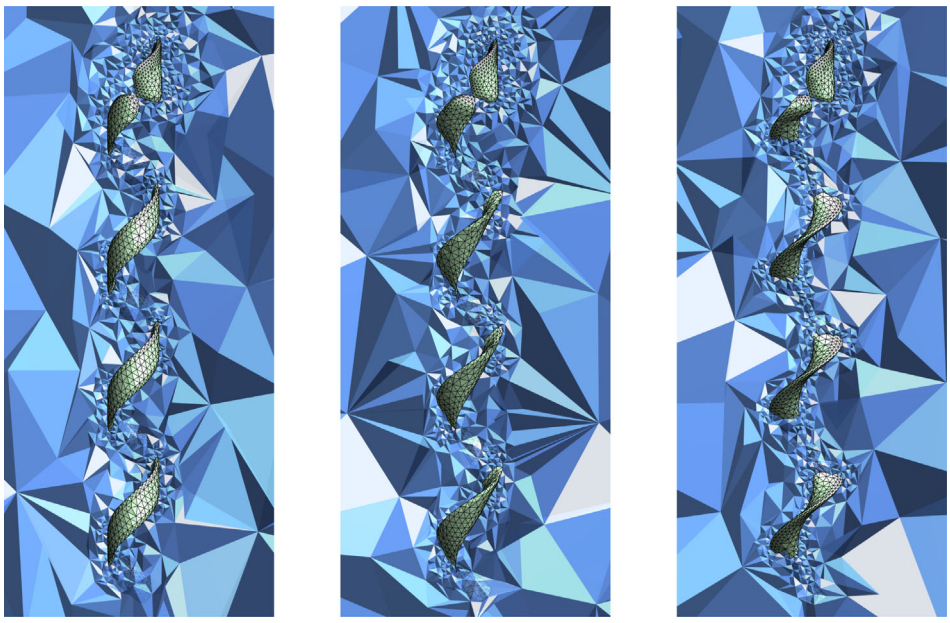

(A) Mesh 1, $\gamma = 0$ (B) Mesh 1, $\gamma = \pi/4$ (C) Mesh 1, $\gamma = \pi/2$

FIGURE 21 Detail of the initial tetrahedral meshes around the microswimmers of Figure 20 [Colour figure can be viewed at wileyonlinelibrary.com]

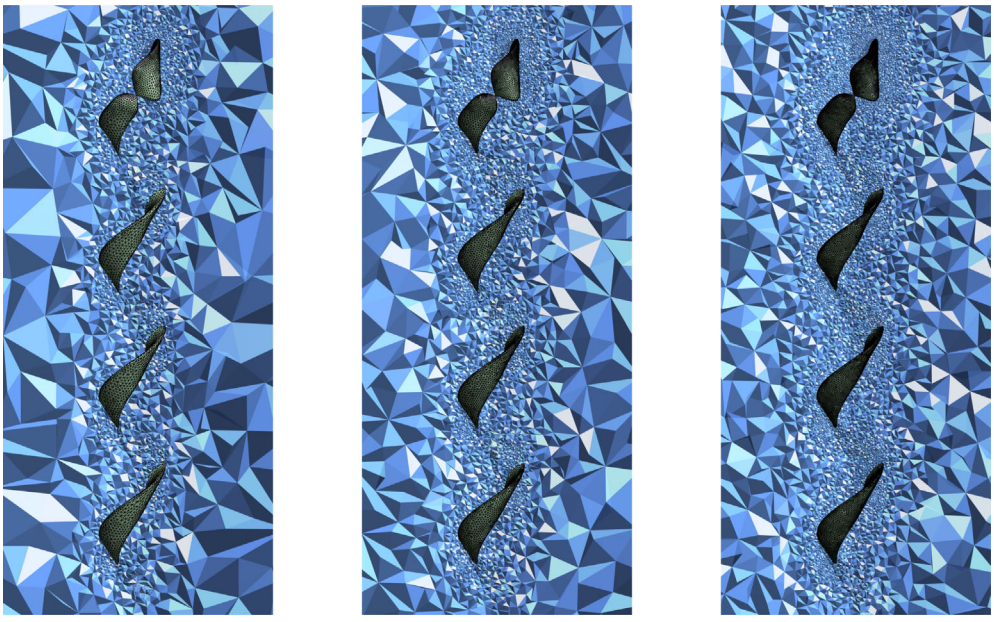

(A) Mesh 3, $\gamma = \pi/4$ (B) Mesh 4, $\gamma = \pi/4$ (C) Mesh 5, $\gamma = \pi/4$

FIGURE 22 Detail of the meshes generated during the automatic mesh adaptive process for the case with initial mesh shown in Figure 21B [Colour figure can be viewed at wileyonlinelibrary.com]

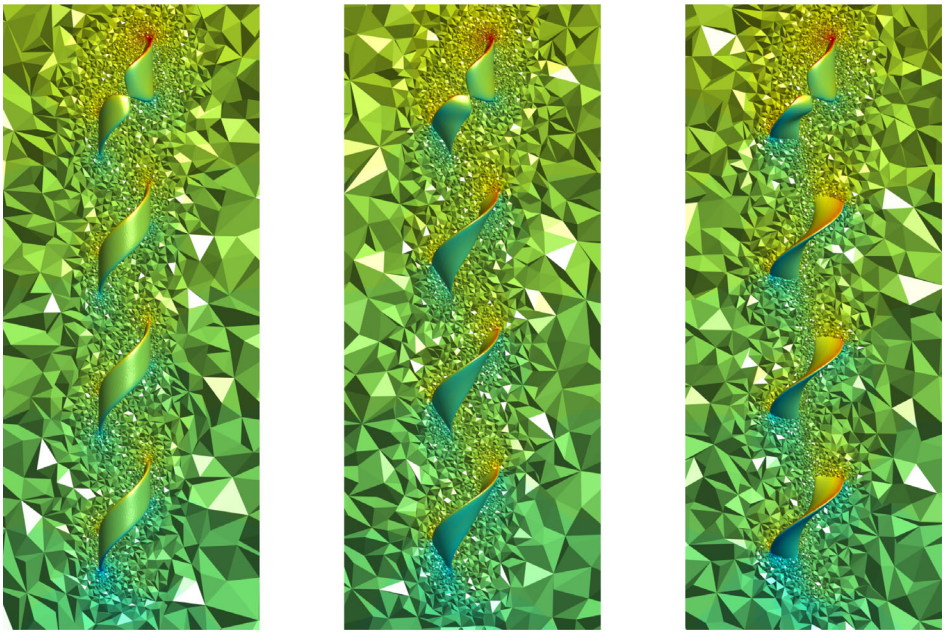

(A) $\gamma = 0$ (B) $\gamma = \pi/4$ (C) $\gamma = \pi/2$

FIGURE 23 Pressure distribution on the fourth mesh for the microswimmers of Figure 20 [Colour figure can be viewed at wileyonlinelibrary.com]

process. The meshes in Figure 22 have (a) 463 342, (b) 1 101 623, and (c) 2 613 300 tetrahedrons, respectively. As it can be observed, the refinement introduced by the automatic mesh adaptivity process concentrates the cells in the regions where the flow is more complex. The size of the corresponding global system to be solved to compute the velocity on the cell faces and the mean pressure on each cell is (a) 3 216 565, (b) 7 662 725, and (c) 18 209 148, respectively.

The pressure distribution on the fourth mesh is displayed in Figure 23. To offer a visual comparison between the three cases, the colour scale is adjusted in the three simulations to be in between −26.60 and 33.24 mPa. The results clearly show the significant variation in the pressure distribution as the geometric configuration, controlled by the parameter γ, is changed. As the value of γ increases the reference area of the body of the swimmer increases, generating higher pressure values in the body for the geometry with $\gamma = \pi/2$ when compared with the geometry with $\gamma = 0$. In all cases, the maximum pressure is observed on the head of the swimmer and the magnitude of the maximum pressure is similar in all three configurations.

Finally, Figure 24 shows the streamlines cultured with the magnitude of the velocity, with a minimum value of 0 μm/s and a maximum value of 4.92 μm/s. The complexity of the flow around the microswimmers can be appreciated as well as the influence of the geometric parameter γ on the flow features.

7 | CONCLUDING REMARKS

This article proposed a formulation of the second-order FCFV method for elliptic problems suitable for application in general meshes of triangular and quadrilateral cells in two dimensions and tetrahedral, hexahedral, prismatic, and pyramidal cells in three dimensions. The computational cost of the resulting problem is comparable to the one of the original first-order FCFV method in terms of number of operations, since in both cases the global unknown is approximated with constant functions on the mesh faces. As in the original FCFV method, optimal first-order convergence of the gradient of the solution is achieved without the need to perform a reconstruction procedure. In addition, when CPU time is compared, the proposed method guarantees an improved approximation of the primal variable, which is now second-order accurate, of almost two orders of magnitude in 3D problems.

The proposed approach also inherits the robustness of the original first-order FCFV method in the incompressible limit. In addition, the proposed method is insensitive to the choice of the type of cells utilised in the discretisation, to their distortion and stretching. More precisely, successful simulations with hybrid meshes were also presented, paving the path towards the application of the discussed methodology to more complex problems requiring boundary layer meshes.

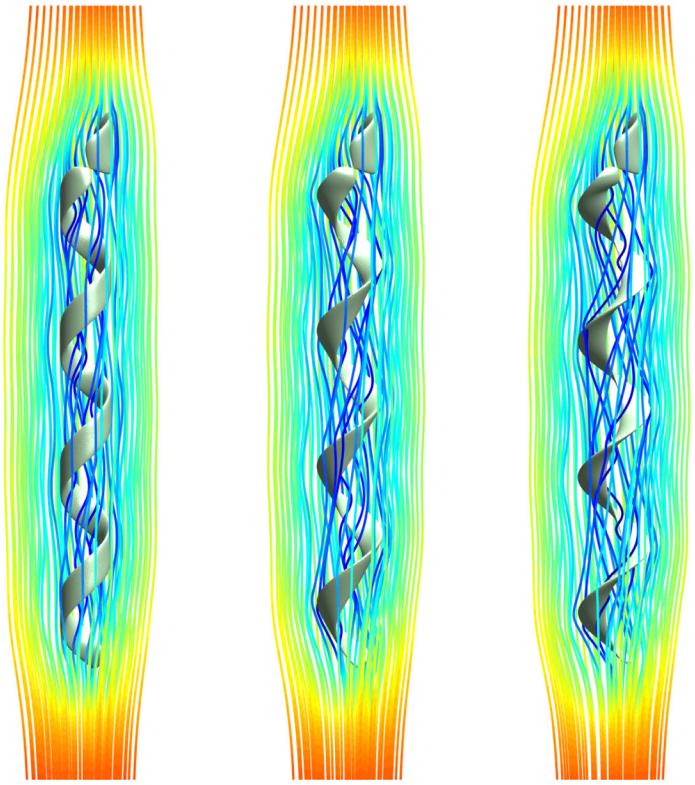

FIGURE 24 Velocity streamlines on the fourth mesh for the microswimmers of Figure 20 [Colour figure can be viewed at wileyonlinelibrary.com]

Finally, an automatic mesh adaptivity strategy is devised by means of a local error indicator obtained via the solution of one extra local problem per cell. The resulting cost of this strategy is thus limited, whereas its advantages are shown in presence of complex geometries and localised phenomenons as, starting from a coarse discretisation, the method is able to automatically construct a set of meshes to achieve a user-defined target accuracy.

Extensive numerical simulations in two and three dimensions are presented to validate the proposed FCFV methodology and the mesh adaptivity procedure. Moreover, a 3D incompressible Stokes problem featuring geometries of interest in microfluidics applications is presented, showing the potential of the method, enhanced by the automatic mesh adaptivity strategy, to treat complex large-scale flow problems.

ACKNOWLEDGEMENTS

This work was partially supported by the European Union's Horizon 2020 research and innovation programme under the Marie Skłodowska-Curie Actions (Grant number: 764636) and by the Spanish Ministry of Economy and Competitiveness (Grant agreement No. DPI2017-85139-C2-2-R). The first author is also grateful for the financial support provided by the Generalitat de Catalunya (Grant agreement No. 2017-SGR-1278). The second authors also acknowledges the support of the Engineering and Physical Sciences Research Council (EP/P033997/1).

CONFLICT OF INTEREST

The authors declare that they have no conflict of interest.

ORCID

Matteo Giacomini https://orcid.org/0000-0001-6094-5944
Ruben Sevilla https://orcid.org/0000-0002-0061-6214

REFERENCES

1. LeVeque RJ. *Finite Volume Methods for Hyperbolic Problems*. Cambridge, MA: Cambridge Texts in Applied MathematicsCambridge University Press; 2002.

2. Eymard R, Gallouët T, Herbin R. Finite volume methods. *Handbook Numer Anal*. 2000;7(7):713-1018. https://www.sciencedirect.com/science/article/pii/S1570865900070058
3. Morton KW, Sonar T. Finite volume methods for hyperbolic conservation laws. *Acta Numer*. 2007;16:155-238.
4. Barth T, Herbin R, Ohlberger M. Finite volume methods: foundation and analysis. *Encyclopedia of Computational Mechanics*. 2nd ed. England, Wiley: Wiley Online Library; 2018:1-60. https://doi.org/10.1002/9781119176817.ecm2010.
5. Cueto-Felgueroso L, Colominas I, Nogueira X, Navarrina F, Casteleiro M. Finite volume solvers and moving least-squares approximations for the compressible Navier–Stokes equations on unstructured grids. *Comput Methods Appl Mech Eng*. 2007;196(45-48):4712-4736.
6. Othmer C. Adjoint methods for car aerodynamics. *J Math Ind*. 2014;4(6) 1–23.
7. Cagnoni D, Agostini F, Christen T, Parolini N, Stevanović I, Falco C. Multiphysics simulation of corona discharge induced ionic wind. *J Appl Phys*. 2013;114(23):233301.
8. Diskin B, Thomas JL, Nielsen EJ, Nishikawa H, White JA. Comparison of node-centered and cell-centered unstructured finite-volume discretizations: viscous fluxes. *AIAA J*. 2010;48(7):1326.
9. Diskin B, Thomas JL. Comparison of node-centered and cell-centered unstructured finite-volume discretizations: inviscid fluxes. *AIAA J*. 2011;49(4):836-854.
10. Sevilla R, Giacomini M, Huerta A. A face-centred finite volume method for second-order elliptic problems. *Int J Numer Methods Eng*. 2018;115(8):986-1014.
11. Cockburn B, Gopalakrishnan J. A characterization of hybridized mixed methods for second order elliptic problems. *SIAM J Numer Anal*. 2004;42(1):283-301.
12. Cockburn B, Gopalakrishnan J. Incompressible finite elements via hybridization. I. the Stokes system in two space dimensions. *SIAM J Numer Anal*. 2005;43(4):1627-1650.
13. Cockburn B, Gopalakrishnan J. Incompressible finite elements via hybridization. II. the Stokes system in three space dimensions. *SIAM J Numer Anal*. 2005;43(4):1651-1672.
14. Cockburn B, Gopalakrishnan J. New hybridization techniques. *GAMM-Mitt*. 2005;28(2):154-182.
15. Cockburn B, Gopalakrishnan J, Lazarov R. Unified hybridization of discontinuous Galerkin, mixed, and continuous Galerkin methods for second order elliptic problems. *SIAM J Numer Anal*. 2009;47(2):1319-1365.
16. Cockburn B, Gopalakrishnan J, Nguyen NC, Peraire J, Sayas F-J. Analysis of HDG methods for Stokes flow. *Math Comput*. 2011;80(274):723-760.
17. Giacomini M, Karkoulias A, Sevilla R, Huerta A. A superconvergent HDG method for Stokes flow with strongly enforced symmetry of the stress tensor. *J Sci Comput*. 2018;77(3):1679-1702.
18. Fu G, Cockburn B, Stolarski H. Analysis of an HDG method for linear elasticity. *Int J Numer Methods Eng*. 2015;102(3-4):551-575.
19. Sevilla R, Giacomini M, Karkoulias A, Huerta A. A superconvergent hybridisable discontinuous Galerkin method for linear elasticity. *Int J Numer Methods Eng*. 2018;116(2):91-116.
20. Sevilla R, Giacomini M, Huerta A. A locking-free face-centred finite volume (FCFV) method for linear elastostatics. *Comput Struct*. 2019;212:43-57.
21. Vieira LM, Giacomini M, Sevilla R, Huerta A. A second-order face-centred finite volume method for elliptic problems. *Comput Methods Appl Mech Eng*. 2020;358:112655.
22. Oikawa I. A hybridized discontinuous Galerkin method with reduced stabilization. *J Sci Comput*. 2015;65(1):327-340.
23. Oikawa I. Analysis of a reduced-order HDG method for the Stokes equations. *J Sci Comput*. 2016;67(2):475-492.
24. Qiu W, Shi K. A superconvergent HDG method for the incompressible Navier-Stokes equations on general polyhedral meshes. *IMA J Numer Anal*. 2016;36(4):1943-1967.
25. Park C, Sheen D. P1-nonconforming quadrilateral finite element methods for second-order elliptic problems. *SIAM J Numer Anal*. 2003;41(2):624-640.
26. Montlaur A, Fernández-Méndez S, Huerta A. Discontinuous Galerkin methods for the Stokes equations using divergence-free approximations. *Int J Numer Methods Fluids*. 2008;57(9):1071-1092.
27. Cockburn B, Dong B, Guzmán J, Restelli M, Sacco R. A hybridizable discontinuous Galerkin method for steady-state convection-diffusion-reaction problems. *SIAM J Sci Comput*. 2009;31(5):3827-3846.
28. Nguyen NC, Peraire J, Cockburn B. An implicit high-order hybridizable discontinuous Galerkin method for linear convection-diffusion equations. *J Comput Phys*. 2009;228(9):3232-3254.
29. Nguyen NC, Peraire J, Cockburn B. A hybridizable discontinuous Galerkin method for Stokes flow. *Comput Methods Appl Mech Eng*. 2010;199(9-12):582-597.
30. Sevilla R, Huerta A. Tutorial on Hybridizable Discontinuous Galerkin (HDG) for second-order elliptic problems. In: Schröder J, Wriggers P, eds. *Advanced Finite Element Technologies*. Vol 566. Switzerland: CISM International Centre for Mechanical Sciences, Springer International Publishing; 2016:105-129.
31. Cockburn B, Di P, Daniele A, Ern A. Bridging the hybrid high-order and hybridizable discontinuous Galerkin methods. *ESAIM: M2AN*. 2016;50(3):635-650.
32. Donea J, Huerta A. *Finite Element Methods for Flow Problems*. England: John Wiley & Sons; England 2003.
33. Cockburn B, Nguyen NC, Peraire J. A comparison of HDG methods for Stokes flow. *J Sci Comput*. 2010;45(1-3):215-237.
34. Díez P, Huerta A. A unified approach to remeshing strategies for finite element *h*-adaptivity. *Comput Methods Appl Mech Eng*. 1999;176(1-4):215-229.

35. Giorgiani G, Fernández-Méndez S, Huerta A. Hybridizable discontinuous Galerkin with degree adaptivity for the incompressible Navier–Stokes equations. *Comput Fluids*. 2014;98:196-208.
36. Sevilla R, Huerta A. HDG-NEFEM with degree adaptivity for Stokes flows. *J Sci Comput*. 2018;77(3):1953-1980.
37. Sevilla R. HDG-NEFEM for two dimensional linear elasticity. *Comput Struct*. 2019;220:69-80.
38. Giacomini M, Sevilla R, Huerta A. Tutorial on Hybridizable Discontinuous Galerkin (HDG) Formulation for Incompressible Flow Problems. In: De LL, Düster A, eds. *Modeling in Engineering Using Innovative Numerical Methods for Solids and Fluids*. Vol 599. Switzerland: CISM International Centre for Mechanical Sciences, Springer International Publishing; Switzerland 2020:163-201.
39. Fořt J, Fürst J, Halama J, Herbin R, Hubert F. *Finite Volumes for Complex Applications VI Problems & Perspectives: FVCA 6, International Symposium, Prague, June 6-10, 2011*. Germany: Springer Science & Business Media; Germany 2011.
40. Karman Steve L., Wyman Nick, Steinbrenner John P. Mesh generation challenges: a commercial software perspective. Proceedings of the AIAA; 2017.
41. Zhang L, Abbott JJ, Dong L, et al. Characterizing the swimming properties of artificial bacterial flagella. *Nano Lett*. 2009;9(10):3663-3667.
42. Keaveny EE, Walker SW, Shelley MJ. Optimization of chiral structures for microscale propulsion. *Nano Lett*. 2013;13(2):531-537.
43. Weatherill NP, Hassan O. Efficient three-dimensional delaunay triangulation with automatic point creation and imposed boundary constraints. *Int J Numer Methods Eng*. 1994;37(12):2005-2039.

SUPPORTING INFORMATION

Additional supporting information may be found online in the Supporting Information section at the end of this article.

How to cite this article: Giacomini M, Sevilla R. A second-order face-centred finite volume method on general meshes with automatic mesh adaptation. *Int J Numer Methods Eng*. 2020;1–29. https://doi.org/10.1002/nme.6428